UCLouvain

FACULTE DES SCIENCES

Faculté des sciences

# Hight-throughput calculations and band engineering on thermoelectric materials

## Volumetric Band Alignment : a way to improve thermoelectric performance.

Auteur : Gabriel Closset

Promoteur : Geoffroy Hautier

Lecteurs : Alexandru Vlad, Gian-Marco Rignanese, Janine George

Année académique 2019-2020

# 1.Table of contents

## 2. Abstract

In the search of new thermoelectric materials, two options are at our disposal: We can either rely on high-throughput screening to discover new interesting compounds or we can enhance those who were previously described in the scientific literature.

In the waiting of a groundbreaking compound, much efforts are dedicated to the improvement of known materials. In this thesis, we will apply one of them, called the Volumetric Band Alignment (VBA), to a few semi-conductors as part of the Material Project[1].

This work will thus be structured as follow:

1) A theoretical review of thermoelectricity aspects and transport properties.

2) The computational methodology of the VBA on an example from the scientific literature ($Ca_2Si$)

3) A selection of candidates in the Material Project Database.

4) The application of the VBA to three half-Heuslers compounds: YNiBi, $MgTe_2$ and LiGaSi.

# Acknowledgment

I would like to thank Geoffroy Hautier, who gave me the opportunity to realize this project, and Francesco Ricci, who supervised me, for their kind support and precious help throughout this entire work.

Besides, I would like to express my sincere gratitude to Olivier Riant and Tom Leyssens for their constant academic and moral support. Words cannot express how grateful I am for your kindness and generosity.

# 3. Introduction

## 3.1 General considerations

The energy consumption remains one of the biggest challenges of the XXI$^{st}$ century. The constant rise of consumption and the steadily decrease of natural resources have altogether set a countdown on the current socio-economic model. And now that oil fields are being drenched out, new alternatives have to be investigated.

Over the past years, most efforts have been conducted to develop and research alternative energies, believed to be inexhaustible (photovoltaic; aeolian; nuclear fusion…). Nevertheless, whatever solution is found, the energy scavenge will always be a major issue. Even if we manage our way to reach a 100% proper and renewable power supply, the waste is unavoidable. For a long-term use, we not only have to reconsider how to produce but also how to use energy.

In all processes, from chemical reactions to electricity transport, a consequent part of energy is always lost. It is well known, for example, that oil combustion is far from efficient energy-wise. In a standard car, the full combustion of 1L of essence does produce ±33MJ of energy. Less than a fourth will actually serve to move the vehicle (14-26%[2]) while the other three quarters will compensate the road friction or disappear in heat transfers. If the frictions can be neglected under specific conditions (using vacuum or magnetic levitation[3]), thermal exchanges will always persist since they are deeply rooted in the thermodynamics laws.

Still, various methods do exist to recover portions of this large waste. One way is the use of thermoelectric materials (further abrv. TE) and their unique property to reversibly convert heat into electricity.

## 3.2 History of thermoelectricity

The concept of thermoelectricity was discovered at the beginning of the XIX$^{st}$ century by Seebeck, Peltier and Kelvin[4] who observed that a gradient of temperature ($\Delta$T) appears at the junctions of two different conductors proportionally to the difference of potential ($\Delta$V) applied to them. This phenomenon is described in the Seebeck-Peltier effect, also called thermopower[5]:

$$\Delta V = S\Delta T \qquad (1)$$

Where S is the Seebeck coefficient.

At the origin of the equation (1), the diffusion of mobile charge carriers inside the materials. Following the temperature gradient, the charge carriers will move from the hot spots to the cold ends, leading to an accumulation of charges in the cold sections. This will result in a net charge that produces an electrical potential[6], as depicted in Fig.1.

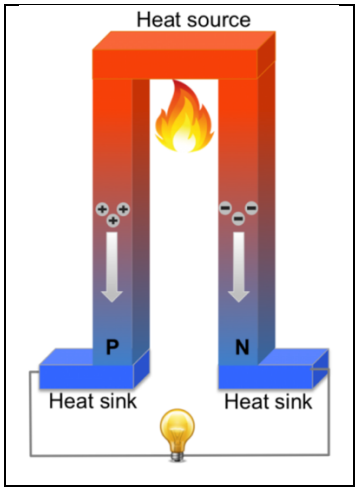


Figure 1 : Schematic representation of a device based on the Seebeck effect.

It is only in 1950 that Abraham Ioffe, a Russian academician showed that semi-conductors were exhibiting TE property[7]. Although this opened new perspectives for energy recovery, only limited progresses were achieved due to the poor performance of TE materials at that time. We have to wait until the nineties and the development of computational chemistry to see a resurgence of interest for TE materials. When theoretical predictions suggested that TE properties in semi-conductors could be significantly enhanced using nanostructural engineering[8].

However, the design for these materials quickly become a brainteaser since it requires the optimization of various conflicting parameters.

## 3.3 The figure of merit

As previously shown in equation (1), the Seebeck coefficient (S) links a difference of temperature ($\Delta$T) to an electric potential ($\Delta$V). To be more specific, it actually measures the specific heat per charge carrier in a material[6]. And since it is an intrinsic property, each compound does possess its own S. The description of this parameter is given in the equation (2) and only applies to metals and degenerated semi-conductors that are heavily doped.

$$S = \frac{8\pi^2 k_b^2}{3eh^2} m^* T . \left(\frac{\pi}{3n}\right)^{2/3} \qquad (2)$$

Where $k_b$ and $h$ the Boltzmann and Plank constants, $e$ the electron charge, $m^*$ the effective mass of charge carrier, $T$ the temperature and $n$ the carrier concentration.[9- 10]

Typical value for Seebeck coefficient varies from a few μV/K in metals to several hundred in semi-conductors (see table 1). For thermoelectric applications, we preferably look for materials with high thermopower (S > 200 μV/K).

*Table 1 : Seebeck coefficients for a few metals and semi-conductors. These values are obtained using $S_{Pt}$ as reference.[11]*

| Metals | Seebeck coefficient (μV/K) | | Semiconductors | Seebeck coefficient (μV/K) |
|---|---|---|---|---|
| Sb | 47 | | Se | 900 |
| Au – Ag - Cu | 6,5 | | Si | 440 |
| Rh | 6 | | Ge | 300 |

Nevertheless, the presence of high S alone is not enough. To evaluate the performance of TE materials, we better refer to the figure of merit (ZT) given by the following expression:

$$ZT = \frac{S^2 \sigma T}{\kappa_{elec} + \kappa_{lattice}} \qquad (3)$$

In addition to the Seebeck coefficient, this score also considers the contributions of both electrical (σ) and thermal (κ) conductivities inside the material. As a matter of convention, we usually refer to $S^2\sigma$ as the Power Factor (abrv. PF).

The thermal conductivity is divided in two parts. In one hand, there is the material lattice contribution ($\kappa_{lattice}$) which parametrizes the atomic vibrations and in the other hand, we have an electrical component ($\kappa_{elec}$), related to the charge carriers. The latter one is strongly correlated to the electrical conductivity (σ) in the Wiedemann-Franz law through the Lorenz factor (L). [6,12]

$$\kappa_{elec} = L\sigma T \qquad (4)$$

Due to the presence of $S^2$, the figure of merit shows a strong thermal dependence that often restrain the use of TE compounds to short temperature ranges[13]. This effect is illustrated in the Fig. 2.

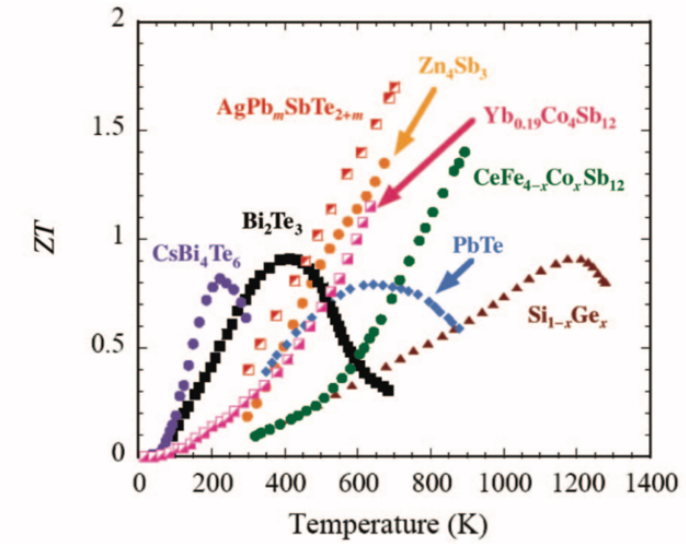


Figure 2 : Figure of merit ZT as a function of Temperature for several bulk thermoelectric materials, adapted from T.Tritt *et al.*[6]

Overall, a ZT greater than 1 can be seen as a prerequisite to reach a conversion rate above 10%[14]. Even if there is no theoretical limit for this value, TE materials rarely display ZT >2 and are expected to become truly competitive when ZT>3 is achieved[15]. The figure of merit provides us a nice view on the TE performances and is also used to measure the energy conversion efficiency. The optimization is thus generally conducted on the figure of merit zT and can be achieved through getting the highest Seebeck coefficient and electrical conductivity for a minimum value of thermal conductivity.

## 3.4 Carrier concentration

The first parameter that could enhance the PF is the carrier concentration (*n*). Unfortunately, this approach is confronted to an intrinsic paradox between the Seebeck coefficient and the electrical conductivity since the carrier concentration impacts S and σ in diametrically opposite manners (see eq. 5).

$$S \propto \frac{1}{n} \qquad \sigma \propto n \tag{5}$$

The correlation between σ and $\kappa_{elec}$ previously mentioned in eq. (4) is part of this problematic but can be considered as a side effect.

A compromise has thus to be found to conciliate large S and σ for a minimal κ. For most semi-conductors, researches show optimal value of power factor when the carrier concentration is about $10^{19}$ to $10^{21}$ carriers/cm$^3$.

Since semi-conductors usually exhibit intrinsic carrier concentration around $10^{10}$ carriers/$cm^3$, heavy doping must be done before reaching the ideal value.

## 3.5 Carrier effective mass

The optimization of the Seebeck coefficient can also be performed on the effective mass (m*) since m* is directly related to S.[16]

$$S \; \alpha \; m^* \tag{6}$$

Before going any further, a distinction has to be made between the total density of state (DOS) effective mass $m^*$ and the effective mass for a single valley in the material bandstructure $m_b^*$. These two parameters are linked one to another in the following expression[17]:

$$m^* = (N_v)^{\frac{2}{3}} \, m_b^* \tag{7}$$

Where $m_b^*$ is the band effective mass and $N_v$, the number of degenerated valleys for charge carriers in the bandstructure. (further described in section 3.7)

As previously noticed in eq. (7), large value of $m^*$ tends to increase the Seebeck coefficient S. It is nevertheless possible to combine high $m^*$ with low $m_b^*$ as it is the case for some well-known TE materials (ie. Bi2Te3, SiGe, BiSb…). Most of these materials offset their poor $m_b^*$ with a high number of band extrema ($N_v$).

However, the effective mass m* also impacts the carrier mobility (μ) which is related to the electrical conductivity (σ) as shown in equation (8):

$$\sigma = \frac{1}{\rho} = ne\mu \tag{8}$$

With ρ the electrical resistivity, *n* the carrier concentration and *e* the electron charge.

The exact physical relationship between the carrier mobility and its effective mass can be summarized as follow[14-18]. Higher values of m* are accompanied by a net decrease of the charge carrier velocity and mobility.

$$\sigma \; \alpha \; \mu \; \alpha \; \frac{1}{m^*} \tag{9}$$

A choice has therefore to be made between the equations (8) and (9) since m* cannot provide high values for both S and $\sigma$ at the same time, just as we previously showed for the carrier concentration.

### 3.6 Lattice thermal conductivity

The last parameter to discuss is the thermal conductivity. As previously shown in eq. (3), the thermal conductivity is composed of an electronic and a lattice component. The electronic contribution comes from the heat transported by electrons and holes, while the lattice part originates from the atomic movements. The vibrations in the 3D structure create waves called phonons that carry heat through the material[14]. This phenomenon is described by equation (10).[6-7]

$$\kappa_{lattice} = \frac{1}{3} C_v v_s \lambda \qquad (10)$$

With $C_v$ the heat capacity, $v_s$, the sound velocity and $\lambda$, the phonon free path.

Although we will not investigate phonons in this work, the lattice thermal conductivity plays an important role in TE design. The first improvements made to ZT consisted in lowering $\kappa_l$ as much as possible. And now that record value of $\kappa_l$ (0,22-0,5 W/mK) have been achieved[12], the main effort is directed towards the improvement of the power factor $S^2\sigma$.

### 3.7 Strategies to improve ZT.

Various methods were developed over the years in order to increase ZT. Here, we will shortly review a few strategies designed to enhance the Power Factor. Other methods do exist for lowering the thermal conductivity ($\kappa$), but they mainly concerned phonon disturbance[19] processes which are once more a bit off track for this work.

#### 3.7.1 Band degeneracy number ($N_v$)

We have to differentiate two concepts: the orbital degeneracy, which occur when bands extrema possess the same energy, and the valley degeneracy ($N_v$), which originate from symmetrical equivalences in the material.

In practice, the value of $N_v$ depends on the number of times a point is repeated by symmetry in the first Brillouin zone. For example, in PbTe, the center position $\Gamma$ has a Nv = 1 while the L and $\Sigma$ points respectively have a Nv = 4 and Nv = 12. (see Fig. 3)

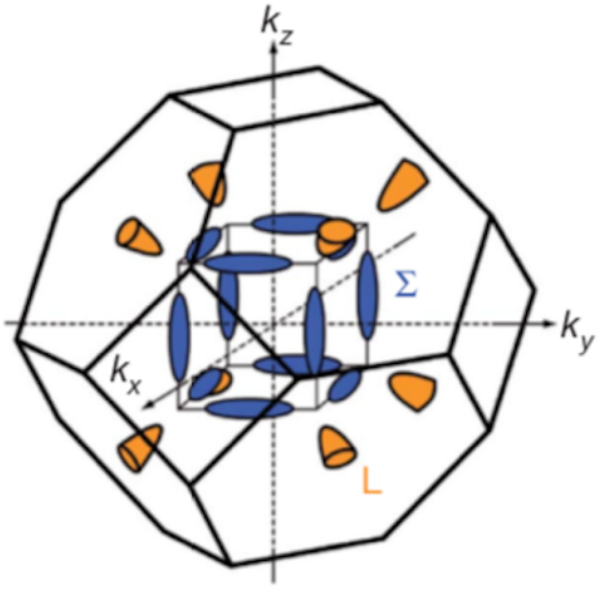


Figure 3 : Valence band structure of PbTe alloy. The figure shows 8 half-pockets at the L point (in yellow) for a number of valley Nv = 4, while the valley degeneracy of $\Sigma$ (in blue) is Nv = 12. Adapted from Snyder *et al.*[20]

The equation (7) showed that the dos effective mass m* depends on the degeneracy level of the bands active in the transport process. To increase this parameter, it is possible to combine the $N_v$ of different bands that are close in energy. This process, also known as band convergence will be fully detailed in section 3.8.

### 3.7.2 Band effective mass ($m_b^*$)

The optimization of $m_b^*$ is made difficult by its opposite contributions to $\sigma$ and S previously evoked. This paradox is especially well illustrated in the bandstructure since $m^*$ can be directly related to the curvature of the bands[21].

So, when a band is flattened (Fig. 4.b), it provides a large value of Seebeck coefficient (S) while a sharp band (Fig.4.a) will be associated to a great electrical conductivity ($\sigma$). This is the reason why a single pocket can hardly provide high Power Factor ($S^2\sigma$).[12]

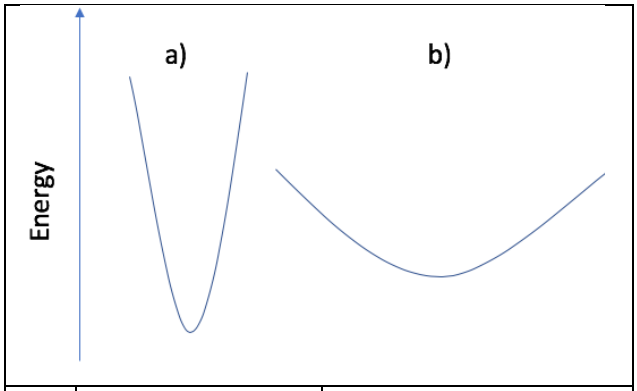


| | | |
|---|---|---|
| m* | ↘ | ↗ |
| S | ↘ | ↗ |
| μ | ↗ | ↘ |
| σ | ↗ | ↘ |

Figure 4 : Impact of the band curvature to m* as well as other TE parameters.

The increase of $m_b^*$ is achieved through distortion in the density of state distribution. Once again, two methods are possible: the band flattening or the use of resonant levels.

In band flattening[22], the $m_b^*$ is modified via the use of dopants with highly localized orbitals. Their presence will lower the orbital overlap and increase the density of state (DOS) near the Fermy level (see Fig. 4.a). A sharp optimization of the carrier concentration is nevertheless required to make the best use of this improvement.[23]

In the other method, resonant levels are induced via element doping in such a way that their additional state lies directly in the host bands. If the newly created levels are at the same energy as the ones already present in the material, they will resonate and create extend states[24]. Such phenomenon will increase the DOS and typically induce a short peak at the resonant energy (see Fig.5.c). The Seebeck coefficient, which depends on the derivative of the DOS, will therefore be boosted.

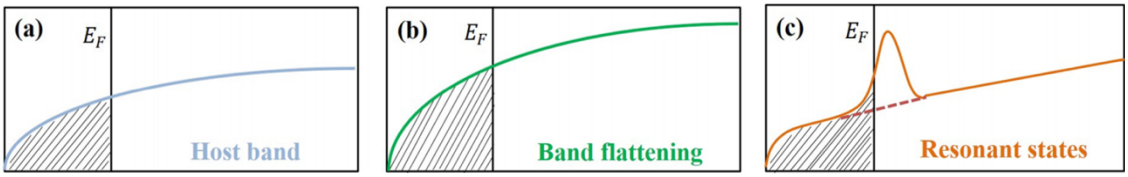


Figure 5 : Schematic representation of the density of states (DOS) in a) a single valence band, b) flattened band, c) with introduction of resonant states. The $E_f$ corresponds to the Fermi Energy. Adapted from Lee *et al.*[22]

### 3.7.3 Carrier scattering and mobility

In TE devices, the charge carriers move from regions with high carrier density to areas where the density is lower. The electrostatic forces cause the carriers to accelerate during their migration whereas collisions with impurities or lattice vibrations tend to stabilize their velocity.

In addition, their overall mobility (μ) is impacted by scattering processes. The scattering rate (τ) is defined by the Matthiessen's rule in eq. (11) as the conjunction of multiple factors ($\tau_i$). Some are caused by crystal defect, such as vacancies or charged impurities, while others are related to lattice vibrations (phonons) or alternative but less current mechanisms. [23,25]

$$\frac{1}{\tau_{tot}} = \sum_i \frac{1}{\tau_i} \qquad (11)$$

It is noteworthy to point out that crystal defects are only predominant at low temperature, they are quickly overcome by phonon scattering when the temperature increases.

In heavily doped TE materials (± $10^{20}$ $cm^{-3}$), the large value for the carrier concentration (±$10^{20}$ $cm^{-3}$) leads to a significant increase of carrier scattering. As a consequence, the carrier mobility is severely reduced.

To improve the PF, one must therefore lessen the carrier scattering. This can be achieved by growing pure crystals structure with a minimal number of defects or by optimizing the dopant distribution inside the material. The creation of undoped area, with low carrier concentration (n) and high mobility (μ), combine with heavily doped sections produce a net diminution of carrier scattering. However, the efficiency of this approach is restrained to low temperature where atom diffusions are slow and phonon scattering is minimal[26]. The doping modulation is illustrated in the next figure.

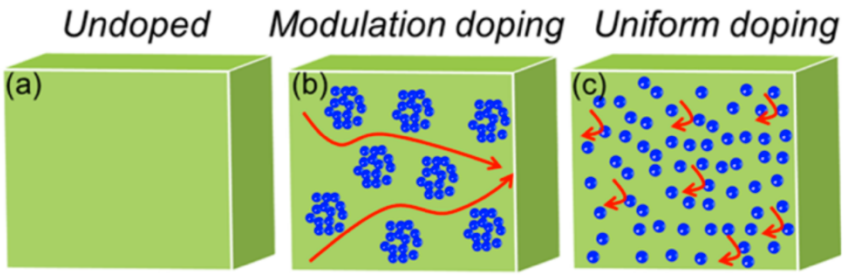


Figure 6 : Schematic representation of carrier mobility across the material. Red arrows show how carriers are scattered by the dopant particles. Adapted from Tan. *et al.*[23]

## 3.8 Volumetric band alignment

The PF enhancement can be performed in many different ways. Among them, figures the Volumetric Band Alignment (abrv. VBA) on which this work is based. We have already explained the challenge around the optimization of *m** and the paradox S/σ that comes with it. It is nevertheless possible to circumvent this issue with the band alignment.

### 3.8.1 Concept

Two extrema points (valleys or pockets, maxima or minima) of a band are aligned when their extremities have an energy difference lesser than $\pm k_b T$[23]. In this case, they form a degenerated state where their respective S and σ are combined as shown in equations (12-13):

$$\sigma_{tot} = \sigma_1 + \sigma_2 \tag{12}$$

$$S_{tot} = \frac{\sigma_1 S_1 + \sigma_2 S_2}{\sigma_{tot}} \tag{13}$$

The new conductivity $\sigma_{tot}$ is given by the direct sum of the individual band conductivities while the Seebeck coefficient is a weighted average. In most cases, the resulting $S_{tot}$ is thus closer to the lowest *S* contribution.

The alignment is particularly efficient on bands with high $N_v$ since they will contribute even more to the total values $S_{tot}$ and $\sigma_{tot}$. Moreover, this method has the benefit to leave *m** unchanged and can be used for both valence and conduction bands. The PF enhancement is therefore performed without any counterparts.

In 2015, the research group of Georg K.H. Madsen[27] demonstrated that such band convergence could be easily achieved with small volume change in the unit cell of some TE materials (see Fig. 7). This approach is called the Volumetric Band Alignment (VBA).

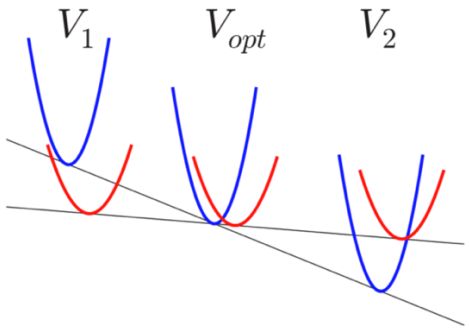


Figure 7: Schematic representation of bandstructure variations when the volume is modified. The $V_{opt}$ corresponds to the ideal volume where two different band edges are aligned one to another. Adapted from Madsen *et al.*[27]

### 3.8.2 Physical origin

The band alignment impact on the PF can be explained through the electronic transport coefficients derived from the Boltzmann transport equation. The physical expressions shown in this section come from the literature.[26-28]

In our case, we start from a linearized version of Boltzmann equation:

$$\sigma(\varepsilon) = \int \boldsymbol{v}_{b\boldsymbol{k}} \times \boldsymbol{v}_{b\boldsymbol{k}} \tau_{b\boldsymbol{k}} . \delta(\varepsilon - \varepsilon_{b\boldsymbol{k}}) . \frac{\mathrm{d}\boldsymbol{k}}{(2\pi)^3} \quad (14)$$

Where $\sigma(\varepsilon)$ is the transport distribution, $\boldsymbol{v}_{bk} = \frac{1}{\hbar^2} . \frac{\delta\varepsilon_{b\boldsymbol{k}}}{\delta\boldsymbol{k}}$, $\tau$ the electron life-time, $\varepsilon$ the band energy, $\boldsymbol{k}$ the wavevector and *b* the band index.

The eq. (14) is used to calculate the moments of the generalized transport coefficients:

$$\mathcal{L}^{\alpha} = q^2 \int \sigma(\varepsilon).(\varepsilon - \mu)^{\alpha}.(-\frac{\delta f}{\delta \varepsilon}).\mathrm{d}\varepsilon \quad (15)$$

Where *f* is the Fermi-Dirac distribution and $\mu$ the chemical potential.

This allows us to express the electrical conductivity and the Seebeck coefficient as declinations of $\mathcal{L}^{\alpha}$ :

$$\sigma = \mathcal{L}^{(0)} \quad (16)$$

$$S = \frac{\mathcal{L}^{(1)}}{qT\mathcal{L}^{(0)}} \quad (17)$$

Both $\mathcal{L}^{(1)}$ and S exhibit significant values when the chemical potential is located in a narrow energy area of a band edge.

So, when two different band (‘ and ‘’) are considered, their PF are combined as follow :

$$PF = S^2\sigma = \frac{1}{q^2T^2}\frac{(\mathcal{L}^{(1)\prime} + \mathcal{L}^{(1)\prime\prime})^2}{\mathcal{L}^{(0)\prime} + \mathcal{L}^{(0)\prime\prime}} \quad (18)$$

And since we can formally write the following equivalences :

$$\mathcal{L}^{(1)\prime\prime} = \alpha_1\mathcal{L}^{(1)\prime} \quad \text{and} \quad \mathcal{L}^{(0)\prime\prime} = \alpha_0\mathcal{L}^{(0)\prime} \quad (19)$$

The PF expression becomes :

$$PF = S^2\sigma = \frac{1}{q^2T^2}.\frac{(\mathcal{L}^{(1)\prime})^2}{\mathcal{L}^{(0)\prime}}.\frac{(1+\alpha_1)^2}{(1+\alpha_0)} \quad (20)$$

And the enhancement only occurs when $(1 + \alpha_1)^2 > 1 + \alpha_0$

Hence, when two pockets with similar m* are aligned in a bandstructure, the requirement previously stated in eq. (20) is fulfilled and the PF increases accordingly.

### 3.8.3 A Literature example: Ca2Si

We present in this section a practical application of the VBA in both Ca2Si and Ca2Ge. The following results are adapted from Madsen *et al.*[27]

Both materials possess three pockets in their bandstructure. They are respectively located in Γ, T, and in the Γ-Y area.

Here, they changed the volume of each compound to bring the pockets as close as possible. The starting situation ($V_0$) is depicted in red while the bandstructure at the optimal volume ($V_{opt}$) is shown in black. The band convergence is also enlightened by arrows in Fig. 8.c) and d).

Next, they computed the transports properties using n-type or p-type doping. The values of PF (in red), S (in blue) are regrouped in Fig. 8 a) and c). They noticed little difference for the p-type doping, represented by a continuous line in Fig. 8, but observed the PF enhancement predicted by the VBA in the n-type situation (dotted line).

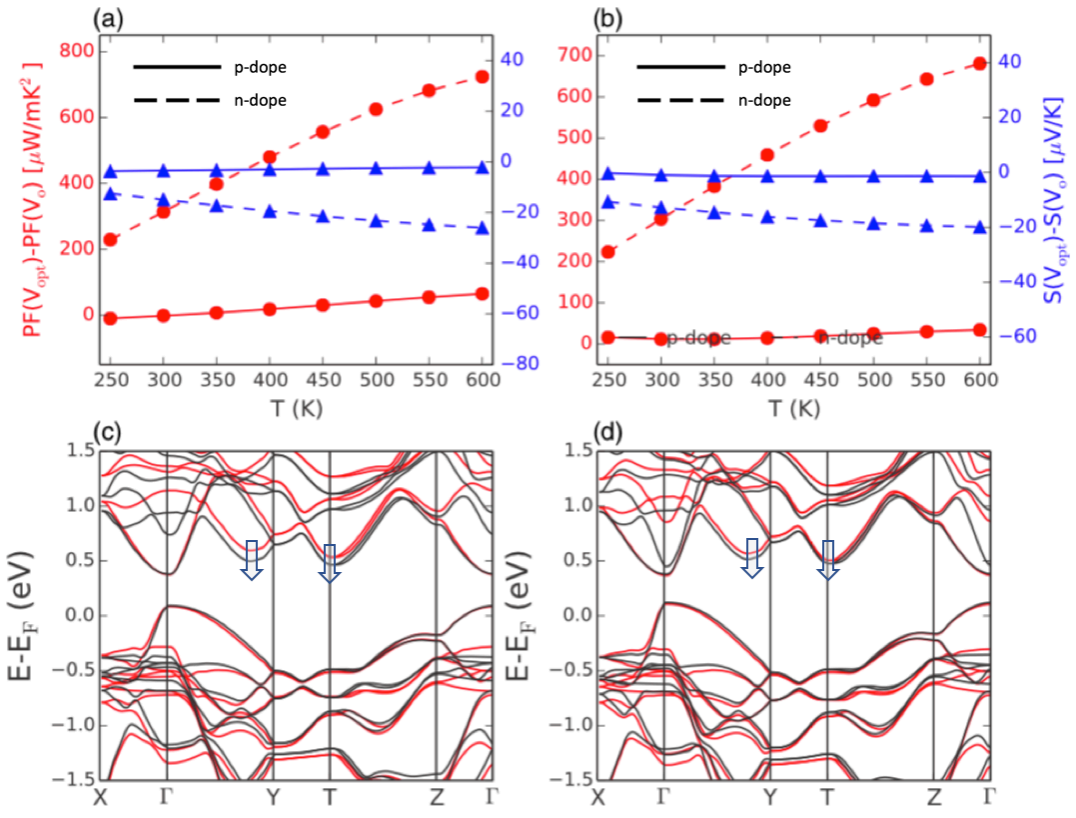


Figure 8 : Bandstructure of $Ca_2Si$ (left) and $Ca_2Ge$ (right) alongside their respective PF and S. Adapted from Madsen *et al.*[27]

At last, it is important to take into consideration the VBA feasibility. In theoretical predictions, we can easily compress or dilate the volume of a unit cell. But in practice, this can only be achieved through alloying or thermal expansion[27]. All the substitution ratios involved in this work will have to be reconsidered in regard to this possibility. Although we limit ourselves to the computational aspect of VBA, it is important to bear in mind the feasibility of this approach.

# 4. Quantum mechanics: from first principal to DFT

## 4.1 The Schrödinger equation

The quantum mechanics has been entirely developed on the basis of the well-known Schrödinger equation:

$$H\psi = E\psi \tag{21}$$

With *H*, the Hamiltonian operator, $\psi$ the wavefunction and *E* the Energy.

As fundamental as the Newton's second law (F=ma) in the history of physics, this equation gives us a complete description of any physical system. This is especially relevant at the atomic level. To avoid the multiplication of variables during its resolution, Max Born and Robert Oppenheimer introduced in 1927 a first approximation. Since the electrons move faster than the nuclei due to the large difference of mass between these particles, the nuclei can be considered as fixed in space and their kinetic energy, neglected. For a system of N electrons, the Hamiltonien can thus be rewritten as:

$$H = \sum_{i=1}^{N}\left(-\frac{1}{2}\nabla_i^2 + v_{ext}(r_i)\right) + \sum_i \sum_{j>i} \frac{1}{r_{ij}} \tag{22}$$

Where the electrostatic potential between an electron (i) and all the protons (M) is depicted in the term $v(r_i)$.

$$v_{(r_i)} = -\sum_{\alpha=1}^{M} \frac{Z_\alpha}{r_{i\alpha}} \tag{23}$$

## 4.2 Hartree

At this stage, the Schrödinger equation can only be solved for hydrogenic systems with no more than one electron. When a second is added, the interaction between electrons does severely complicate the calculations. To overcome this difficulty, some additional approximations have to be made.

In the Hartree approximation, the original wave function is split into single particle functions so that each of them only considers one electron at a time. The poly-electronic system is then considered as a product of well distinctive hydrogenic systems. (see eq. 24)

$$\psi(r_1, r_2, \dots r_n) => \phi_1(r_1).\phi_2(r_2).\dots\phi_n(r_n) \tag{24}$$

In the Hartree approximation, the resolution is mathematically exact but also inaccurate since we severely underestimate the electron-electron interaction.

The Hartree functions can be depicted as follow:

$$\varepsilon_i \phi_i(r_i) = \left( -\frac{1}{2}\nabla_i^2 - \sum_i \left( \frac{Z_I}{|r_i - R_I|} \right) + \sum_{i \neq j} \int \frac{\phi_j^*(r_j)\phi_j(r_j)}{|r_i - r_j|} dr_j \right) \phi_i(r_i) \quad (25)$$

## 4.3 Hartree-Fock and anti-symmetry

Within the Hartree approximation, the spin of the electrons was first omitted from the calculations. To parametrize its effect on the all system, an "exchange" condition was added to the equation (26). This constrains the electrons in the same orbital to have a different spin (+1/2 or -1/2) and to thereby respect the anti-symmetry principle.

$$\varepsilon_i \phi_i(r_i) = \left( -\frac{1}{2}\nabla_i^2 - \sum_i \left( \frac{Z_I}{|r_i - R_I|} \right) + \sum_{i \neq j} \int \frac{\phi_j^*(r_j)\phi_j(r_j)}{|r_i - r_j|} dr_j \right) \phi_i(r_i) - \sum_{i \neq j} \int \frac{\phi_j^*(r_j)\phi_i(r_j)}{|r_i - r_j|} dr_j \, \phi_j(r_i) \quad (26)$$

## 4.4 History of DFT[29]

The calculations that rely on the Hartree-Fock approximation were not only inaccurate but also time consuming. These two parameters led to the development of new approaches for the resolution of the Schrödinger equation. Among them figure the *density functional theory* (DFT).

In atomic systems, the energy can be generally seen as the sum of three different components: the kinetic energy of the electrons (T), the electronic repulsion between them ($U_{ee}$) and the attraction with the protons from the nuclei ($U_{eN}$).

$$E = T + U_{eN} + U_{ee} \quad (27)$$

Unfortunately, none of these parameters can be directly measured or observed. For this reason, Thomas and Fermi proposed in 1927 to rewrite them on the basis of the electron density, which is a much more accessible physical value.

$$E \approx C_f \int \rho(r)^{\frac{5}{3}} . dr + \int \rho(r) V_{ext} . dr + \frac{1}{2} \int \frac{\rho(r)\rho(r')}{|r - r'|} . dr dr' \quad (28)$$

They encountered a limited success since they were unable to find a suitable expression for the kinetic contribution and carried on a huge imprecision on it. Besides, they could not include the exchange term in their new energy description.

We have to wait until 1964 for Hohenberg and Kohn to prove that an electron density-based method could replace the usage of a wavefunction.

By demonstrating that two different atomic systems cannot exhibit the same electronic density as long as they stay at their ground state, they enlightened the fact that one electron density p(r) could only lead to one Hamiltonian, one wavefunction and therefore, one energy ($E_0$).[30]

$$\rho(r) \rightarrow V_{ext} \rightarrow H \rightarrow \psi(r_1, r_2, \dots r_n) \rightarrow E_0 \tag{29}$$

Therefore, a direct link can be established between the electron density p(r) and the ground state energy of the system ($E_0$). They also chose an elegant way to overcome the problems previously encountered when using this approach. Instead of trying to parametrize quantities they could not formally relate to the electron density (id est: the exchange, the kinetic contribution and the $e^-$-$e^-$ repulsion), they regroup them under a single term ($F_{HK}$) that could remain undeveloped. The ground state energy could be rewritten as depicted in equation (30):

$$E_0(\rho_0) = \int \rho_0\,(r) V_{ext}.\, dr + F_{HK}(\rho_0) \tag{30}$$

By applying a variational approach to $E_0$, it then became possible to minimize the electron density until it reached its ground state value. And all this, without knowing exactly the detail of $F_{HK}$.

$$E_0 \leq E(\overline{\rho}) = \int \rho_0\,(r) V_{ext}.\, dr + F_{HK}(\rho_0) \tag{31}$$

In comparison to the Hartree-Fock method, one could say that Hartree relies on an exact expression that gives an approximate result while the DFT uses an approximate expression to provide a nearly exact result[31].

## 4.5 Application of the DFT

The treatment of the exchange-correlation term ($F_{HK}$) represents the last hurdle for a practical use of the DFT. Although its energy contribution ($E_{xc}$) cannot be accurately described, it is still possible to estimate its value. Different methods exist. Among them, figure the local density approach (LDA) and the generalized gradient approximation (GGA). In the first assumption, the real $E_{xc}$ is replaced by the $E_{xc}$ of a uniform electron gas that possess the same electron density. The second approach additionally considers the local variations of the electron density. Since atomic systems are actually inhomogeneous, this last option is slightly closer to the reality.

Even if the DFT supplants the Hartree-Fock methods in term of computational speed as well as in accuracy, it still cannot provide an exact energy due to the approximations made for $E_{xc}$ and tends to severely underestimate the band gap in electronic bandstructures.[32]

This fact has led to the development of new hybrid functional (B3LYP, PBE0 etc.) that combines various level of theory to compensate their respective weaknesses and increase their degree of precision.

Since the DFT shows good results when applied to the study of solids and metallic compounds, all the calculations presented in this work were done using this method.

# 5. Methods

## 5.1 Softwares

### 5.1.1 The Vienna ab initio simulation package (VASP)

Most calculations realized as part of this work were done on the basis of the VASP package. This computer program applies the first principles of quantum-mechanic to perform a large variety of simulations, such as molecular dynamic and electronic structure calculations.

In practice, VASP resolves the many-body Schrödinger equation[33] using various level of theory: the density functional theory (DFT) by resolving the Kohn-Sham equations; the Hartree-Fock (HF) approximation by solving the Roothaan equations; or using both through hybrid functionals.

To work properly, the VASP program needs 5 different input files which are hereby shortly described:

-The INCAR file, where the parameters for the calculation are set, eg the energy cut-off, the number of self-consistent loops, the functional that will to be used…

-The POSCAR file, which contains the composition and the structure of the compound.

-The POTCAR file, that contains the list of pseudopotentials linked to each atom of the compound. These data are based on the projector augmented wave method (PAW) and are more convenient for this kind of ab-initio calculations.

-The KPOINTS file, where a k-points mesh is set to describe the reciprocal space.

-The submitting script, to manage the computational time and resources allocated to the calculation.

### 5.1.2 The BoltzTrap code

BoltzTrap2[34-35] is a software designed to calculate transport properties from material bandstructures. The program actually relies on a Fourier expansion to resolve the Boltzmann transport equation in the rigid bond approximation. This prevents bandstructure alterations when different temperature or doping levels are considered[36].

In addition, the relaxation time ($\tau$) can also be modulated within BolzTrap2. During our calculations, we used the constant relaxation time approximation to remove the usual thermal and energy dependences of $\tau$. Hence, The Seebeck coefficient no longer dependents of $\tau$ while the electrical conductivity will show a linear relation with it.

## 5.2 Computational methodology for VBA

When trying to apply the VBA to a new material, we proceed in 3 steps:

-First, we compute the bandstructure for different volume of the same unit cell and see if the band edges inside the pockets can be put closer one to another.

-Secondly, from the variations inside the bandstructure, we know if we need to compress or dilate the structure to reach the optimal volume ($V_{opt}$) where PF should be maximized.

-Lastly, we generate a supercell for the compound and we introduce some changes in the structure, by replacing some light atoms by bigger one, to reach the desire volume $V_{opt}$. A supercell can be understood as the juxtaposition of unit cells to form a bigger system with more atoms but the same properties. In practice, we use a 2x2x2 supercell to have a sufficiently large system to do slight substitutions and volume changes. Moreover, since the substitutions must not alter too much the chemistry of the material (i.e. atomic bond, bandstructure …), the replacing atoms are chosen in the same family as the original ones.

## 5.3 Computational setup and resources

Each material was fully relaxed before launching a static run and computing the bands. The calculations were done using the projected augmented wave (PAW) pseudopotentials provided by VASP[37]. All computations were performed using DFT GGA functional and an energy cutoff of 520 eV, as suggested in the VASP inputs available on Material Project[1], on the CECI-CISM cluster Lemaitre3[38] hosted at the Université catholique de Louvain-la-Neuve. The transport properties were computed within the BoltzTrap2[28] software.

The various scripts used along this thesis originate from Pymatgen[39] (Python Materials Genomics), a robust and open-source Python library for materials analysis with high support for VASP. Moreover, both Pymatgen and sumo-master[40] interfaces were used to realize graphic interpretations.

# 6. Results and discussion

## 6.1 Computation of Ca2Si alloys

### 6.1.1 Objective

To illustrate the Volumetric Band Alignment (VBA) methodology, we start this work with an application to Ca2Si alloys. Since this example has already been fully described by Madsen *et al.*[27], all we will do here is reproducing results from the scientific literature.

As a start, they conducted a screening over 3000 M-X combinations (see Fig. 9) of semi-conductors. They isolated the thermodynamically stable structures with good thermoelectric score (zT > 0,4) and chose 8 candidates to test the VBA. One of the remaining materials was the $Ca_2Si$. This choice was quite convenient since $Ca_2Si$ can be easily mixed with Ge or Sn, which show a chemistry similar to Si, through alloying.

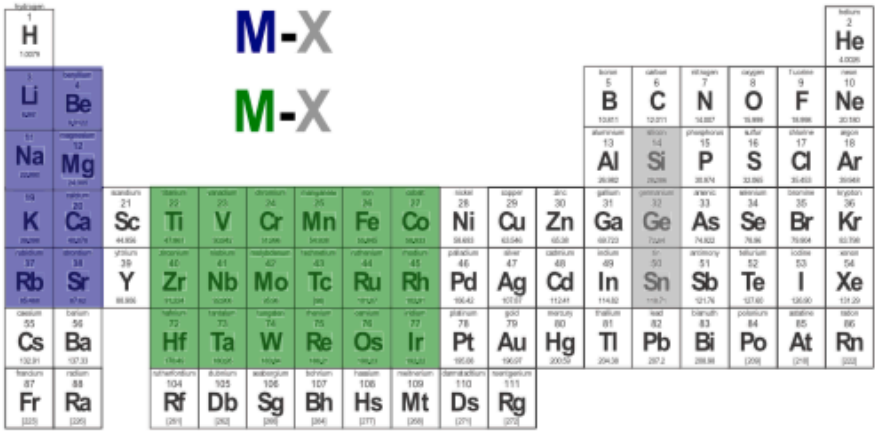


Figure 9 : List of M-X materials investigated to test the VBA. Adapted from Madsen *et al.*[27]

For some materials that went out of their screening, we ran our own calculation to see if we can reach the same results as theirs and also to familiarize ourselves with the VBA methodology.

### 6.1.2 Pocket alignment and rise of the PF

Starting from the orthorhombic $Ca_2Si$ (mp-2517 in the material project database[1]), we fully relaxed the structure and computed its bandstructure. The unit cell of $Ca_2Si$ is represented in Fig. 10 and contains 12 atomes (8 Ca and 4 Si).

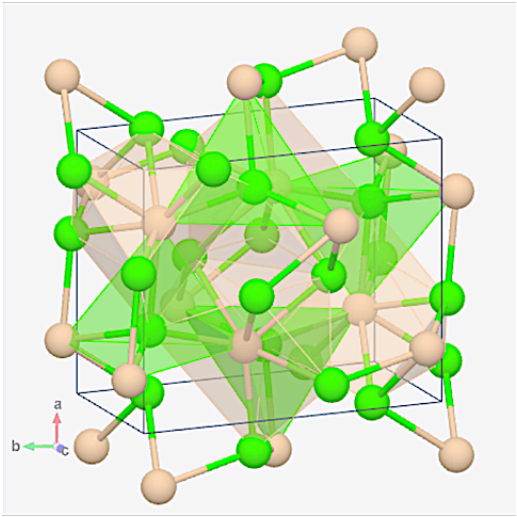


Figure 10 : Structure of orthorhombic Ca2Si (space group: Pnma) from the Material Project Database. Ca are in green and Si in beige.

In the bandstructure this material, we can clearly discern three pockets (indicated by arrows in Fig. 11) respectively located in Γ, U and somewhere between Γ-X in the conduction band.

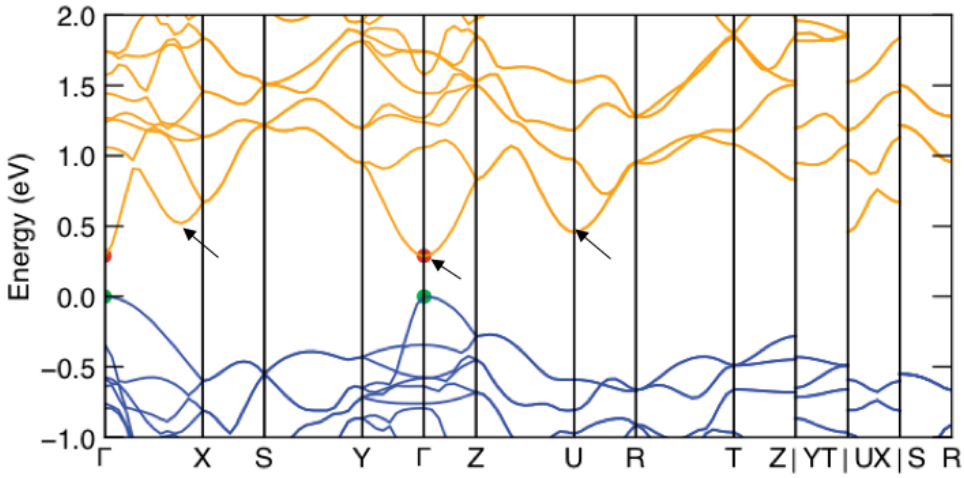


Figure 11 : Bandstructure[40] of Ca2Si. Band-edges are in red for the conduction band (in yellow) and in green for the valence band (in blue).

We notice that the three pockets are at different energy levels. To see if we can bring them closer with the VBA, we have to define how each of these three points reacts under a change of volume. We thus modified the original volume of $Ca_2Si$ unit cell ($V_0$) for various ratios (x), as depicted in eq. (33).

$$V = V_0 \pm x.V_0 \qquad (32)$$

So, when we use the label V+5%, it means that the volume of the material unit cell has been increased by 5% of its original value.

After that, we recalculated the bandstructures for new volumes with ratios x= 2%, 5%, 10%, 20%. The impact on the pockets distance is shown in Fig. 12. The red point at 332,05Å$^3$ corresponds to the original volume of $Ca_2Si$ ($V_0$).

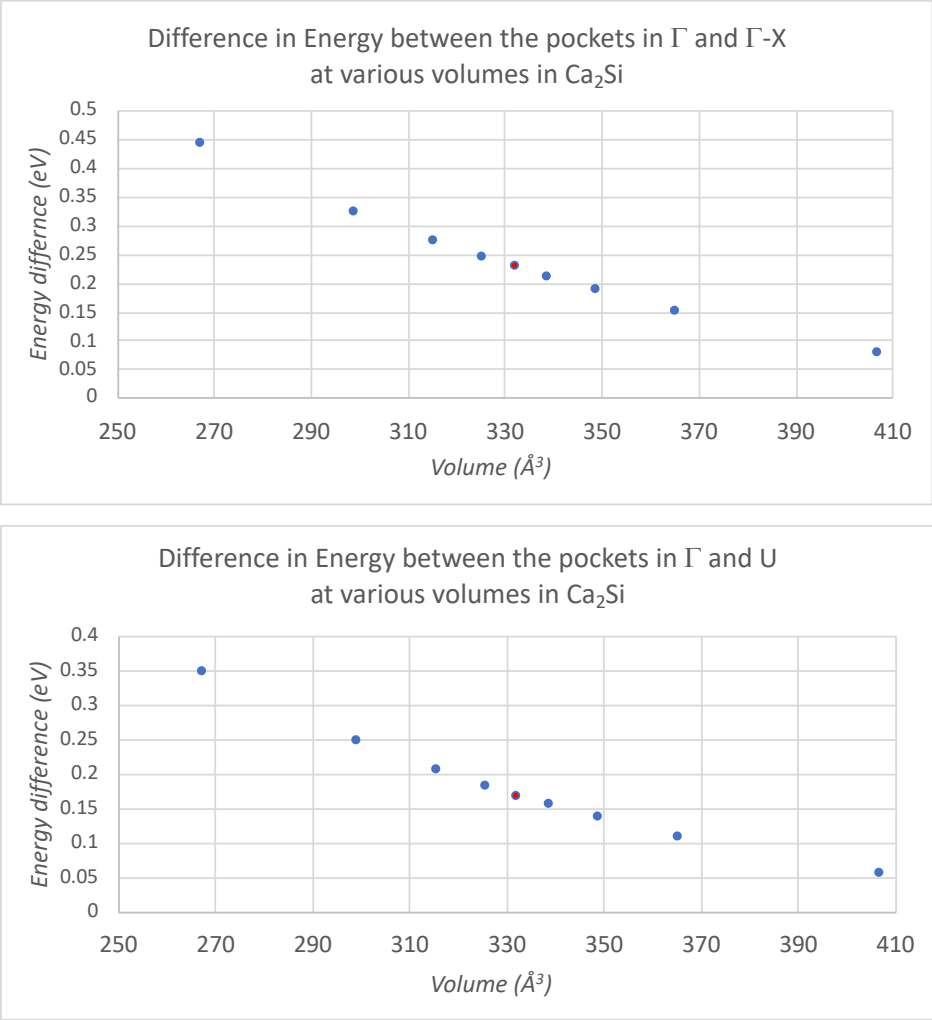


Figure 12 : Energy dependence of the 3 pockets under a change of volume. The point in red at 332,05 Å$^3$ corresponds to the original volume of $Ca_2Si$ ($V_0$).

Since the energy of each pocket seems to converge when the volume of the cell increases, one can reliably think that the electronic transport coefficients will undergo the desire modifications. If this is the case, it means that the VBA approach works just as expected. We thereby looked at the electrical conductivity, the Seebeck coefficient (S) and the power factor (PF) across the different volumes that were previously used.

To carry on with these measures, we set the carrier concentration to $10^{20}$ cm$^{-3}$ and calculated the PF with *n-doping*. Results show a clear improvement in the Fig. 13.

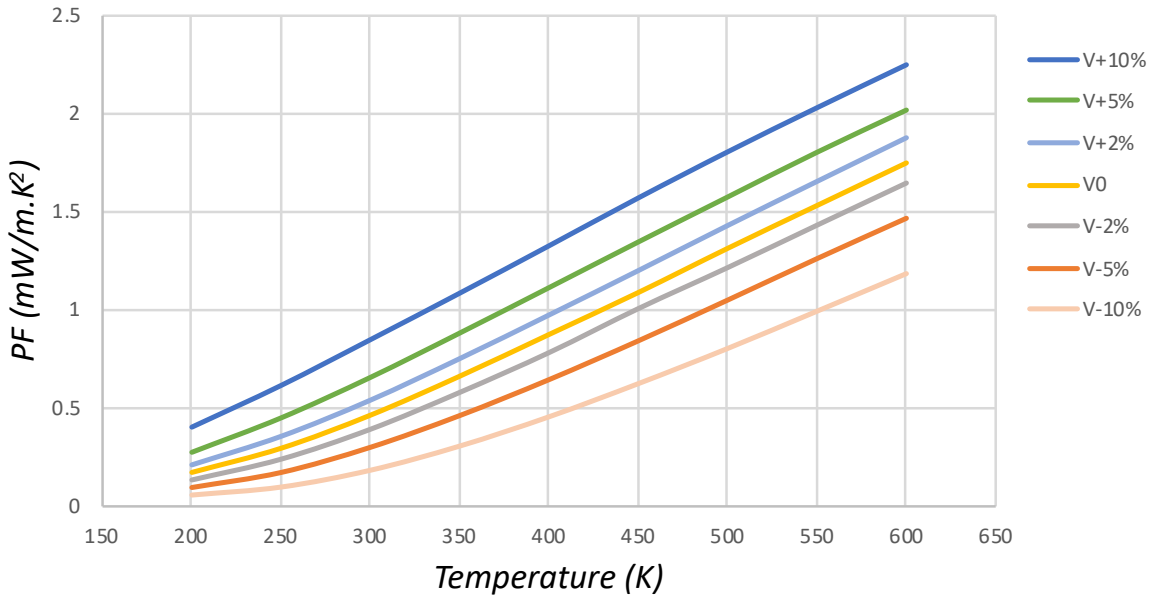


Figure 13 : Power factor as a function of Temperature for various volume of cell in $Ca_2Si$ with a *n-type* doping and a carrier concentration of $10^{20}$ $cm^{-3}$.

From the Fig. 13, we can clearly confirm that the PF increases steadily with the Volume, alongside the Seebeck coefficient and with a drop of electrical conductivity (see annex B for the details of S and σ). These results comfort the idea that the main goal of the VBA has been reached. The ideal Vopt, where the distance between all three pockets is minimized, should be located somewhere beyond V+20%.

### 6.1.3 Volume increase by atomic substitutions

Now that we have the confirmation that the PF of Ca2Si can be improved through volumetric modification, we can start replacing atoms. To do so, we stayed with the proposition of the study[27] and we substitute some silicon (Si) with Germanium (Ge) and Tin (Sn) which do not alter the bandstructure of the alloy to severely. We will thus compute and compare three different $Ca_2X$ systems (X = Si, Ge, Sn) and three intermediate alloys $Ca_2X_{1-n}X'_n$. It is also noteworthy to mention that $Ca_2Sn$ has already been proposed as a TE material[41]. The respective volumes and formation energy for the 6 systems are listed on the Fig. 14.

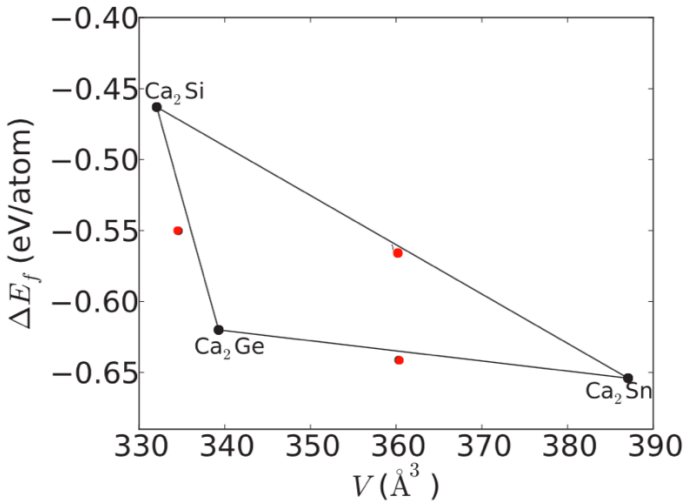


Figure 14 : Formation energy and volume for different $Ca_2X$ systems. The points in red represent the intermediate systems $Ca_2X_{1-n}X'_n$ we will investigate. Adapted from Madsen *et al.*[27]

The systems can be sorted by increasing order of volume:

$$Ca_2Si < Ca_2Si_{0,75}Ge_{0,25} < Ca_2Ge < Ca_2Si_{0,75}Sn_{0,25} < Ca_2Ge_{0,75}Sn_{0,25} < Ca_2Sn$$

And one could expect the pocket convergence and PF to follow the same tendency.

### 6.1.4 Impact on the bandstructure

*$Ca_2X$ systems*

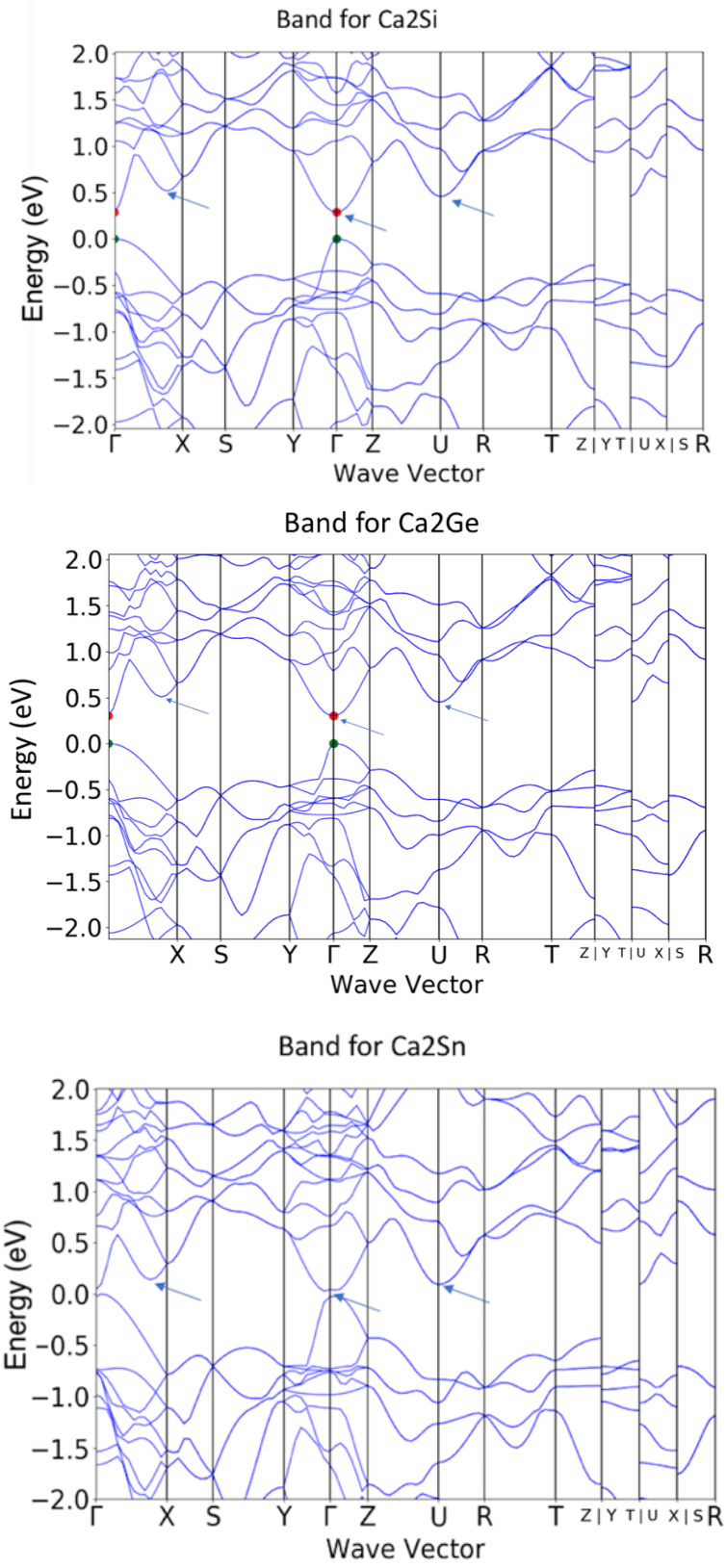


Figure 15 : Bandstructure of $Ca_2Si$, $Ca_2Ge$ and $Ca_2Sn$. The pockets of interest are enlightened with arrows.

The profile around the band gap remains the same in the three systems. We still have a direct band gap centered on Γ and two other pockets, respectively located in U and Γ-X. The relative distance between the pockets are regrouped in the table 2.

Table 2 : Pocket convergence in $Ca_2X$ compounds (X=Si, Ge, Sn).

| Material | Distance (eV) Γ / Γ-X | Distance (eV) Γ / U |
|---|---|---|
| $Ca_2Si$ | 0,2298 | 0,1687 |
| $Ca_2Ge$ | 0,2062 | 0,1521 |
| $Ca_2Sn$ | 0,0936 | 0,0466 |

The $Ca_2X$ materials are sorted by increasing order of volume (Si<Ge<Sn). The pocket convergence occurs, just as expected, when the unit cell is expanded. It is particularly visible for $Ca_2Sn$, which possesses the highest volume.

*$Ca_2X_{1-n}X'_n$ systems*

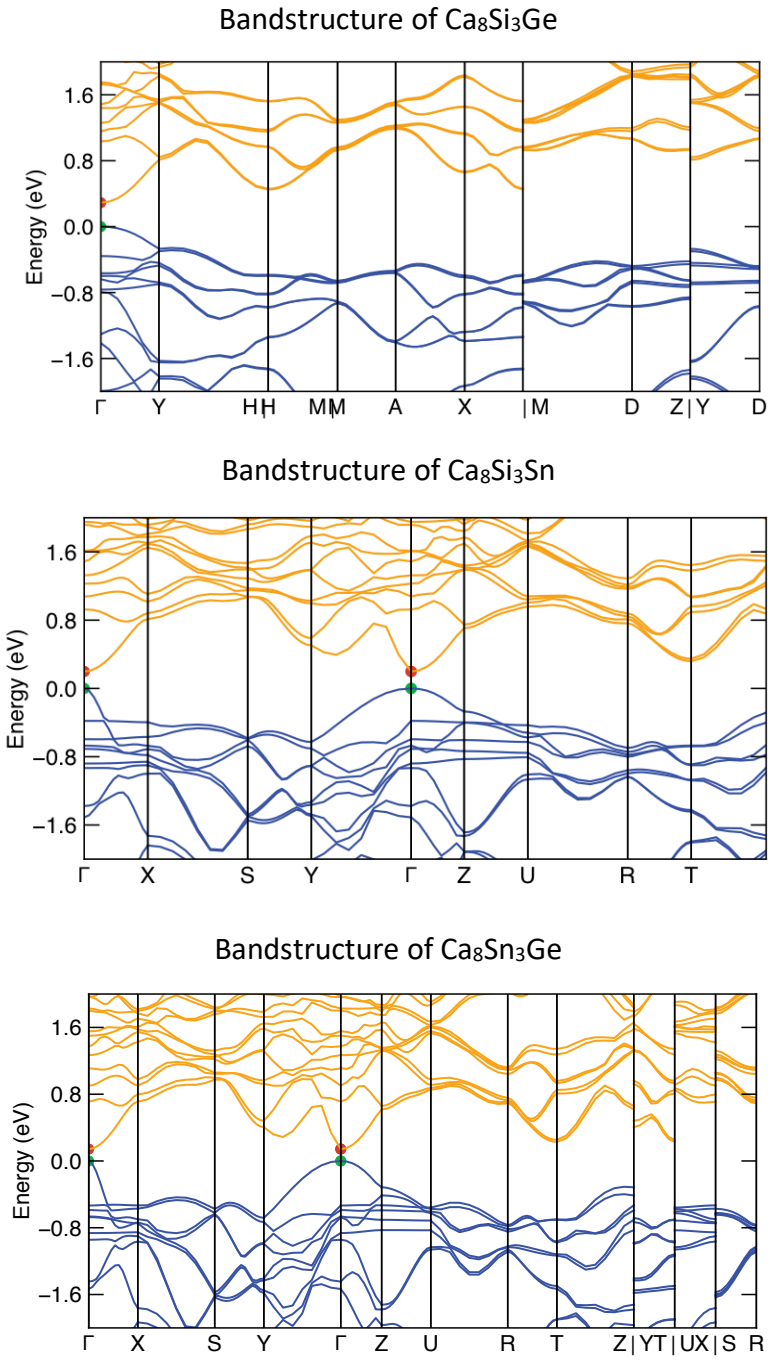


Figure 16 : bandstructure of mixed alloys $Ca_2X_{1-n}X'_n$ with n=0.25.

We chose to replace 25% of the Si by another atom to get some test compound along the edges of the triangle previously depicted in Fig. 14. The proper way to proceed should be to determine first which ratios are allowed by the thermodynamic and see if they are reachable through alloying. Here, we limited ourselves to a single value of 'n' to see how the substitution

would alter the bandstructure and the power factor. However, this ratio was also proposed in the paper of Madsen *et al.*[27] as one possibility.

The use of a 2x2x2 supercell to compute these alloys can alter the path of the bandstructures. It then become harder to compare the pockets in the respective materials since we do not longer know their exact position. One could assume that the pocket in Y-Γ corresponds to the previous Γ-X and that the pocket in U is now shifted in T position. The pockets distances are combined in table 3.

*Table 3 :* Pocket convergence in $Ca_2X_{1-n}X'_n$ compounds (X=Si, Ge, Sn), with n=0,25.

| Material | Distance Γ / Y-Γ | Distance Γ / T |
|---|---|---|
| $Ca_8Si_3Ge$ | N/A | N/A |
| $Ca_8Si_3Sn$ | 0,1720 | 0,0984 |
| $Ca_8Sn_3Ge$ | 0,1470 | 0,0871 |

The $Ca_2X_{1-n}X'_n$ materials are, once again, sorted by increasing order of volume (Si<Ge<Sn). We can only compare the last two compounds since the $Ca_8Si_3Ge$ bandstructure is built on a completely different path. The pocket convergence seems nevertheless to occur when the unit cell is expanded. From the results of Madsen *et al.*[27], we know that it is actually the case. To ensure this fact, one could compare the Fermi surfaces or reconstruct the original path (the same that is used for $Ca_2Si$) for the bandstructures.

### 6.1.5 Impact on the power factor

The three $Ca_2X$ compounds are sensible to the VBA, since it is possible to improve their power factor by doping their structure with heavier atoms. In each case, the substitution from $Ca_2X$ towards $Ca_2X_{1-n}X'_n$, with larger volume, has led to an improvement of PF. Overall, the shift Si -> Sn appears to be the most effective approach. In Fig. 17, we pool together the PF for the different alloys computed.

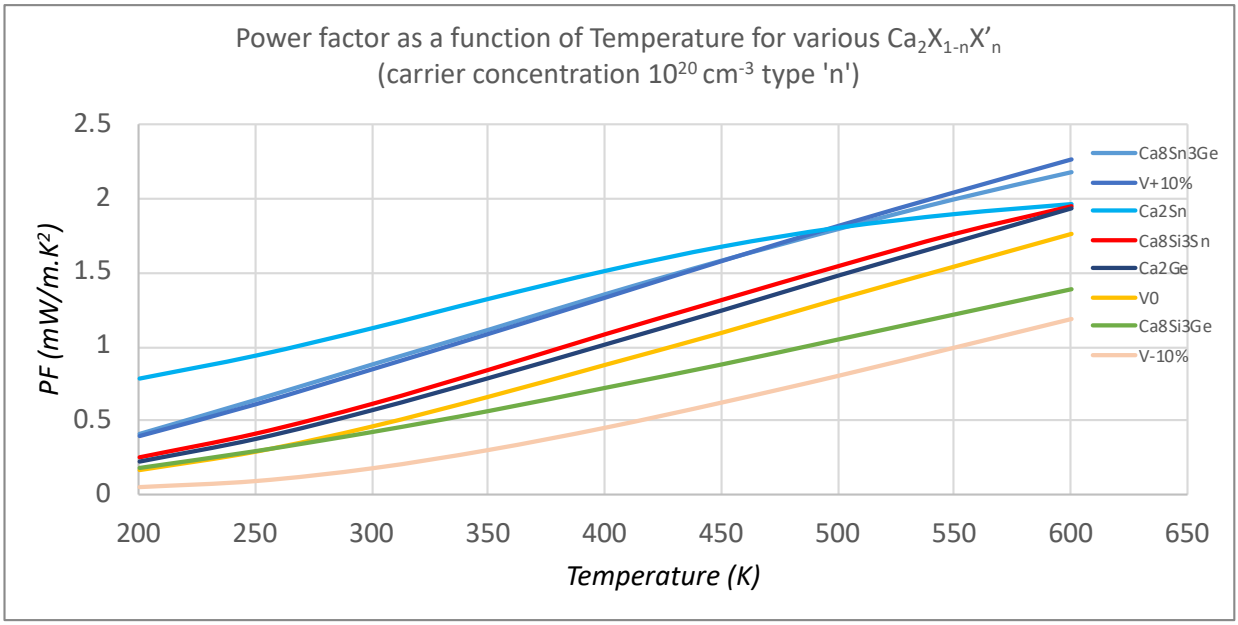


Figure 17 : Power factor of various alloys. The V0, V+10% and V-10% referred to the pure $Ca_2Si$ compound depicted previously (in Fig. 13) and is used here as a reference.

The $Ca_2Si$ based-systems exhibit a strong response to the VBA and can be pulled off as a nice example to illustrate the method. As previously mentioned, the PF enhancement follows the volume increase with one exception. The volume difference between Ca2Si (332,05 $Å^3$) and $Ca_2Si_{0,75}Ge_{0,25}$ (334,81 $Å^3$) is too low (>1%) to improve the PF (see Fig. 17 in green).

These compounds are quite convenient since the $V_{opt}$, where all the three pockets are aligned, can be experimentally reached through alloying[27]. The PF enhancement can thus be pushed to its maximum. Although, we have no guarantee to expect the same behavior when working on other TE compounds.

## 6.2 Application to new materials

### 6.2.1 First selection

To test the VBA, we had a shortened list of candidates in Table 4. These materials are part of the Material Project[1] and come from the analysis of a dataset of band extrema of strained materials developed by the Modeling group (MODL) of the Institute of Condensed Matter and Nanosciences (IMCN) at the université catholique de Louvain-la-Neuve (UCL). They picked amoung cubic materials those that show high degeneracy number and band convergence.

Table 4 : List of TE candidates for the VBA with the location of their pocket. A screening in the material project[42] database established a shortened list of TE materials that are likely to respond to the VBA.

| Formula | type | % strain | First pocket | Second pocket | Degeneracy | ΔE(p1-p2) (ev) |
|---|---|---|---|---|---|---|
| YNiBi | n | 2 | X | Γ | 4 | 0,068 |
| LiGaSi | n | 2 | X | L | 7 | 0,056 |
| MgTe2 | n | 2 | Γ | Γ-R | 9 | 0,030 |
| LiZnP | n | 2 | X | Γ | 4 | 0,006 |
| Li2CuSb | n | 2 | X | L | 7 | 0,123 |
| Mg6Bi2PN | p | 2 | Γ | X | 4 | 0,054 |
| Na3SbSe4 | n | 2 | H-N | Γ | 2 | 0,249 |
| ThNiSn | p | 2 | X | Γ | 4 | 0,138 |

Since we don't have the time to investigate each compound in detail, we will focus our attention on the more promising one. We first prioritize materials with a high degeneracy (cfr section 3.7.1) that are thermodynamically stable. That leaves us with three candidates: YNiBi, LiGaSi and $MgTe_2$. The main interest is to see if these new candidates are responsive to the VBA.

### 6.2.2 Pocket alignment and PF enhancement

Just as we did for $Ca_2Si$, we start looking if the pockets can be brought closer by changing the volume for the three candidates. We reused the formalism depicted in eq. (33) to generate volumes with a 2% and 5% change compared to $V_0$. After computing the bandstructure for each compound, we measured the energy for each pocket and compiled the ΔE between them in the following graphics.

LiGaSi

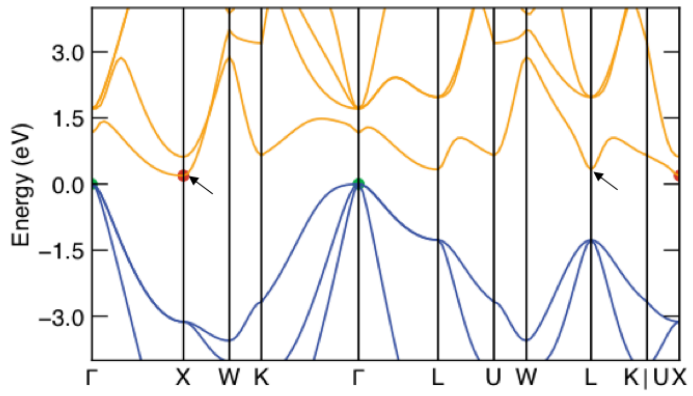


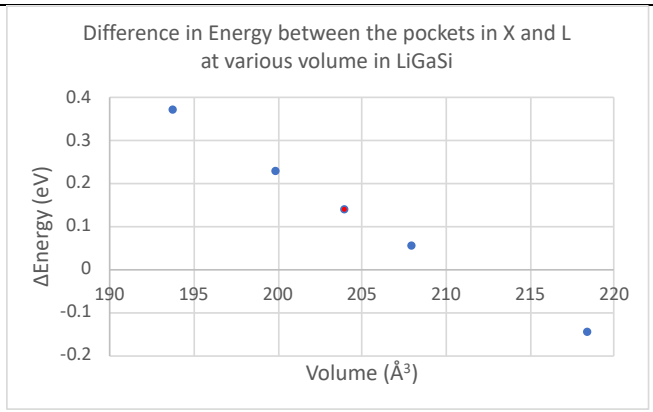


$MgTe_2$

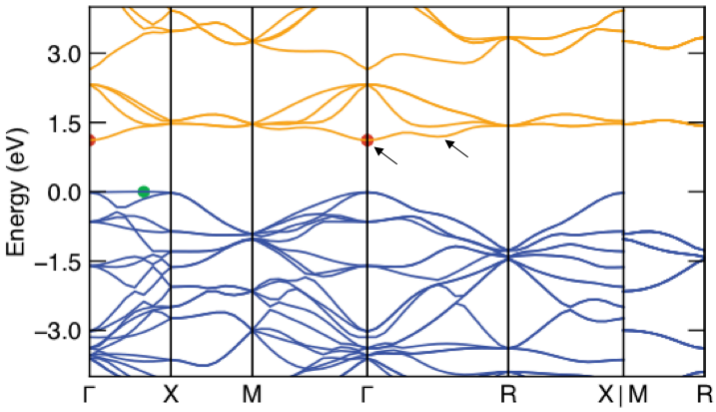


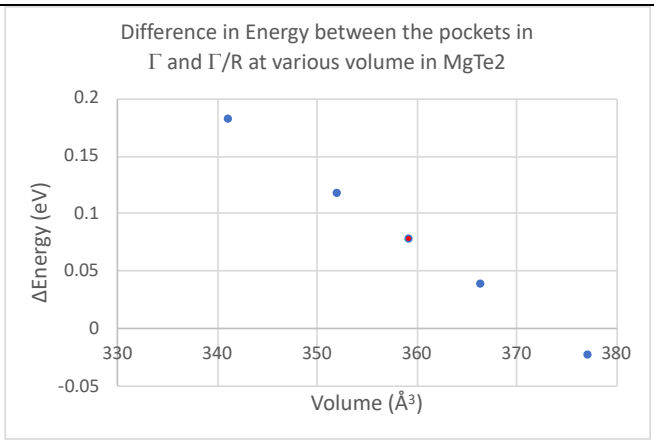


YNiBi

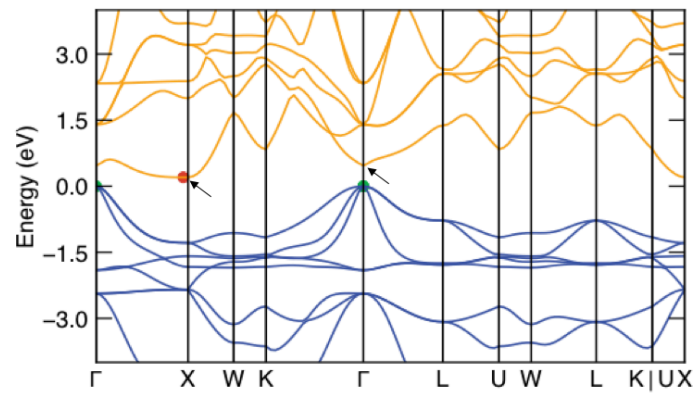


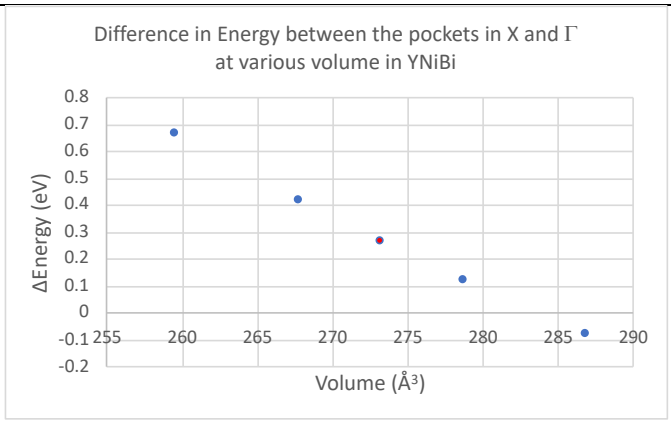


Figure 18 : Left are compiled the bandstructures of the three candidates at their original volume $V_0$ and right, the energy dependence of the pockets under a change of volume for each compound. The points in red correspond to $V_0$. Detailed results and DOS plots are shown in annex D.

After computing the bandstructure of LiGaSi, YNiBi and $MgTe_2$, we observed a smooth pocket alignment in each material when the volume is slightly increased (see Fig.18). The negative values observed for V+5% mean that, at this volume, the two pockets invert their order in energy.

From the pocket convergence graphs, we are also able to interpolate the $V_{opt}$ in each case through a simple linear regression.

Table 5 : $V_0$ and theoretical $V_{opt}$ for each of the three materials.

| | $V_0$ | $V_{opt}$ |
|---|---|---|
| LiGaSi | 203,99 | 210,67 |
| $MgTe_2$ | 359,26 | 371,19 |
| YNiBi | 273,21 | 283,28 |

Then, for each volume, we computed the PF and its dependencies. As settings, we used a carrier concentration of $10^{20}$ $cm^{-3}$ and a temperature range between 200K and 600K. The evolution of the Seebeck coefficient (S) and the conductivity ($\sigma$) can be found in annex E.

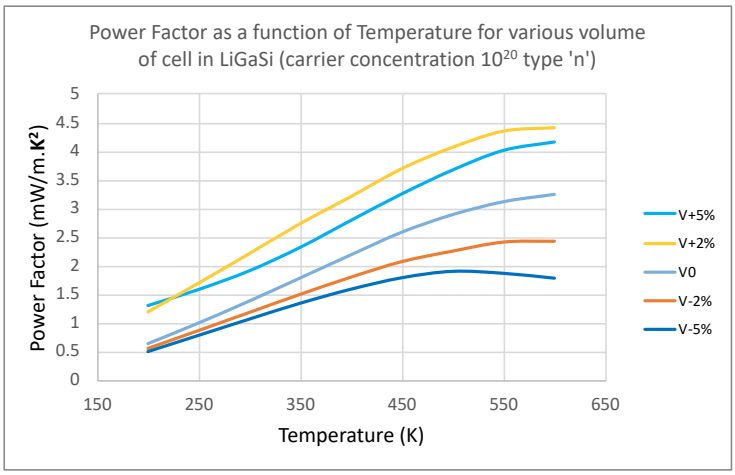


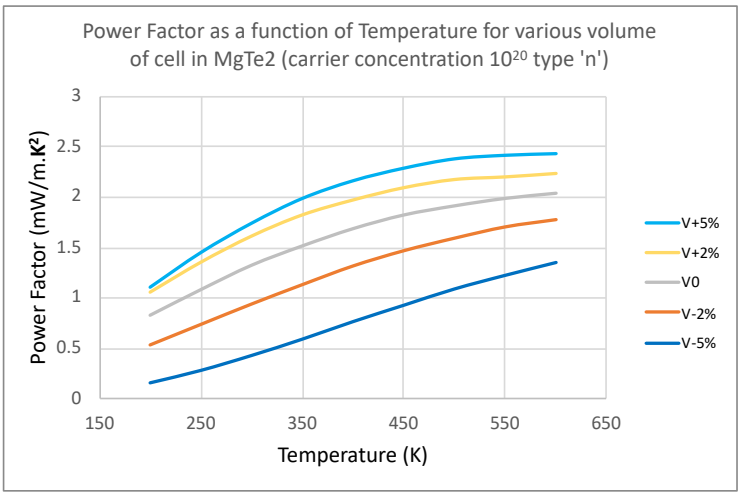

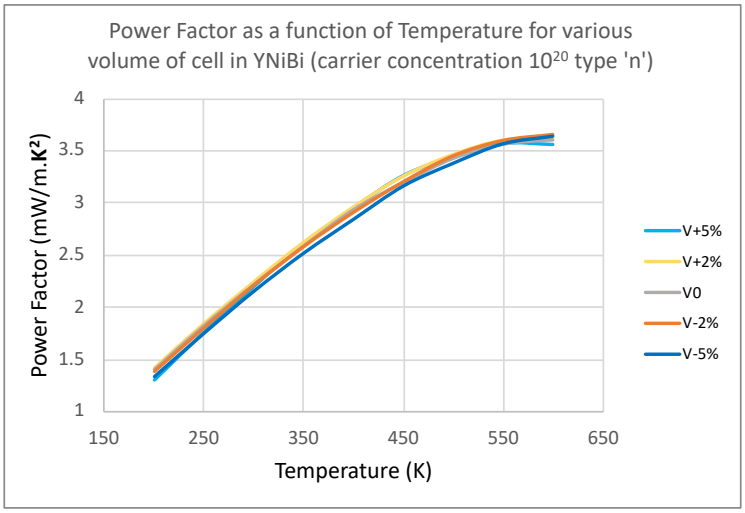


Figure 19 : Variation of PF in LiGaSi, MgTe2 and YNiBi under a change of volume.

In both LiGaSi and $MgTe_2$, the PF is strongly impacted by the volumetric change. The PF rises up when the volume increases until a certain point where he starts decreasing. This point located somewhere in between V+2% and V+5% should actually correspond to the $V_{opt}$ previously calculated.

### 6.2.3 A word about the no-response of YNiBi

Despite being a nice candidate on the paper, with a pocket shape bandstructure and an acceptable band degeneracy of 4, there is no sign of PF improvement in YNiBi. The apparent inefficacity of the VBA on YNiBi is intriguing. As it was the candidate with the less degeneracy (vs: degeneracy of 7 for LiGaSi and 9 for MgTe2), one could assume that the PF enhancement in this material should be weaker but still present.

To have a better understanding of this case, we rerun the PF calculation, but with a carrier concentration of $10^{19}$ and $10^{21}$ carrier/$cm^3$ since the previous results were computed only for $10^{20}$ carrier/$cm^3$.

Power Factor for YNiBi

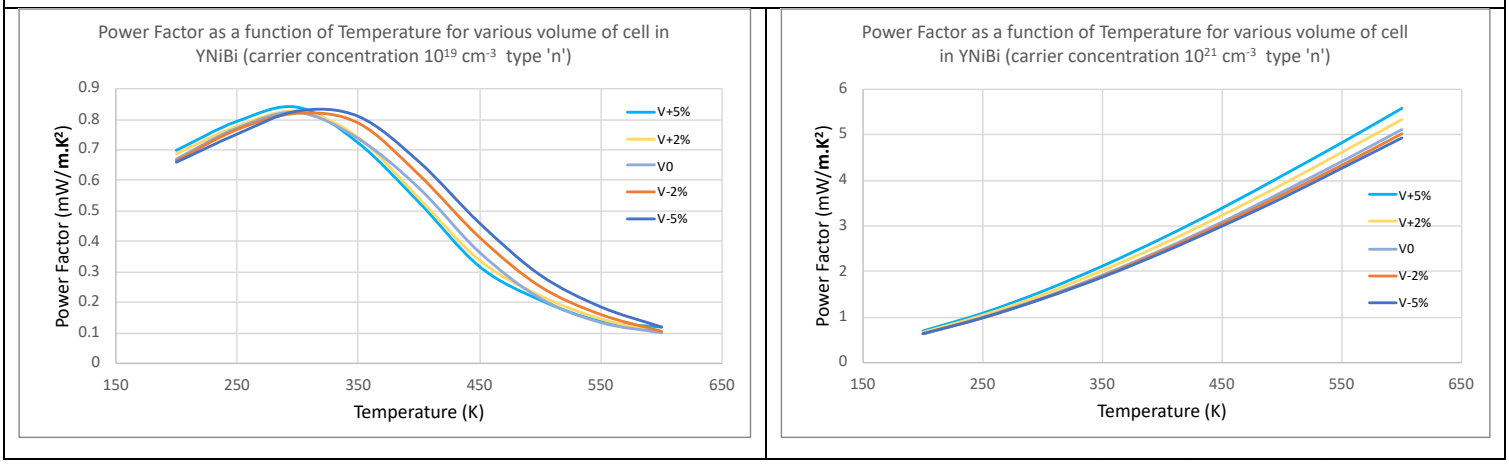


*Figure 20: Power Factor for YNiBi at various volumes with carrier concentration of $10^{19}$ and $10^{21}$ carrier/cm$^3$.*

As shown in the Fig. 20, it is finally with a carrier concentration of $10^{21}$ carrier/cm$^3$ that we are able to notice the improvement predicted by the VBA. The PF enhancement is way smaller than the one observed for LiGaSi and $MgTe_2$ but still present. This effect appears when higher carrier concentrations are used. Since most TE materials need a carrier concentration between $10^{19}$ - $10^{21}$ carrier/cm$^3$ in order to maximize the power factor, we stay here with reasonable values.

When looking at the nice convergence in energy of the pockets in YNiBi, one could expect this compound to exhibit a strong response to the VBA. Nevertheless, the PF enhancement is really poor in YNiBi compared to the other two materials. We hereby return to the bandstructures of YNiBi to see if we can explain this phenomenon.

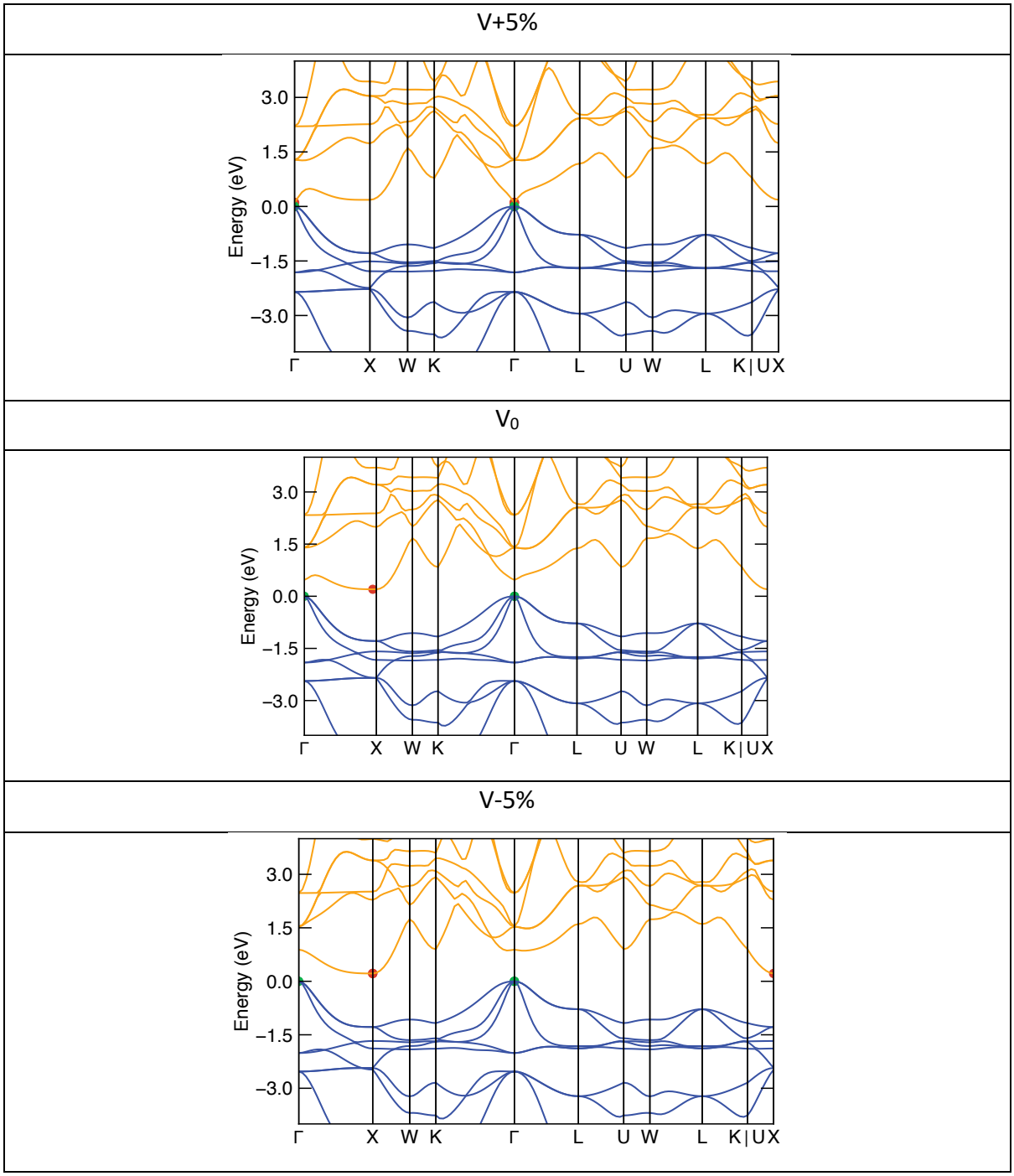


Figure 21 : Bandstructures of pure YNiBi at various volume of cell. The pockets of interest are respectively located in X and Γ.

From these bands, we notice that the VBA has a strong impact on the Γ point but seems to have little effect on the rest of the bandstructure in YNiBi. When decreasing the volume, the Γ valley is shifted up and the distance between the pockets located in X and Γ become slightly bigger. Since this situation does not really differ from the one observed at $V_0$, it is reasonable to acknowledge that the PF happen to be nor better or worse in this situation.

To explain the poor response of YNiBi, we thus advance the argument of a band-gap closure (see section X.X). When increasing the volume, the $\Gamma$ valley can be lowered in such a way that the already tiny band-gap at this point (0,26 eV) is quickly shortened. The pocket alignment can therefor provoke a band-gap closure that goes with a loss of semi-conductivity.

This particular case illustrates well the limitation of the VBA and we have to ask ourselves which level of improvement can be reached without losing the semi-conductivity. In order to determinate the exact limit of PF enhancement, one would need to closely investigate the evolution of the band-gap under volume changes. And here, we are unfortunately confronted to the theoretical limits of DFT calculations[32]. Other level of theory, such as hybrid functionals, are required to conduct these analyses. Since this would drive us away from the purpose of the VBA, we limit ourselves by just pointing this out.

## 6.3 A case study: LiGaSi

### 6.3.1 Pocket alignment

In this section, we will restrain ourselves to the study of one TE material. Since we are able to investigate less substitutions in $MgTe_2$ compared to LiGaSi, we opted to work with the latter. The results from the previous section show that the VBA works fine in LiGaSi and that the pockets of interest (X and L) do converge well when the volume is increased. By chance, the volume changes also lower the value of the $\Gamma$ valley which could be aligned with the other two pockets. This phenomenon has little influence since the $\Gamma$ pocket contributes the less to the global PF due to its degeneracy of 1. Even so, the alignment of a third pocket is convenient and come thus as a bonus (see Fig. 22).

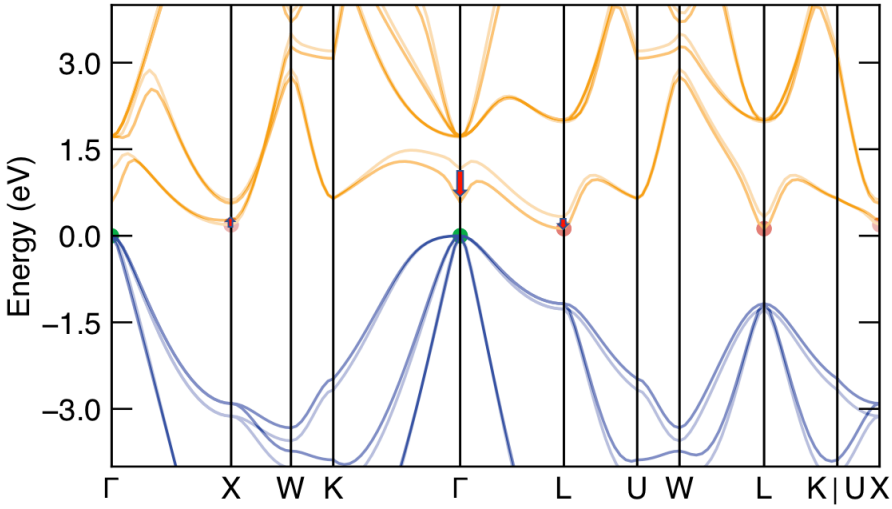


*Figure 22 : Bandstructures of LiGaSi at $V_0$ in light, and V+5% in bold. The pockets in X and L in the conduction band are shifted one the another along with $\Gamma$.*

### 6.3.2 Density of state

Concerning the substitutions, we have a very large choice when it comes to replace atoms in LiGaSi. Whatever the changes may be, we need to be sure that the substitution does not drastically alter the shape of the bandstructure. As we search to improve the PF in the material, it would be painful to completely change its nature.

At this point, it would be more than useful to know precisely how each atom contributes to the bandstructure, especially around the pocket's locations at 0,19 eV (X) and 0,33 eV (L). In order to do that, we computed the density of state (DOS) for LiGaSi (see Fig.23).

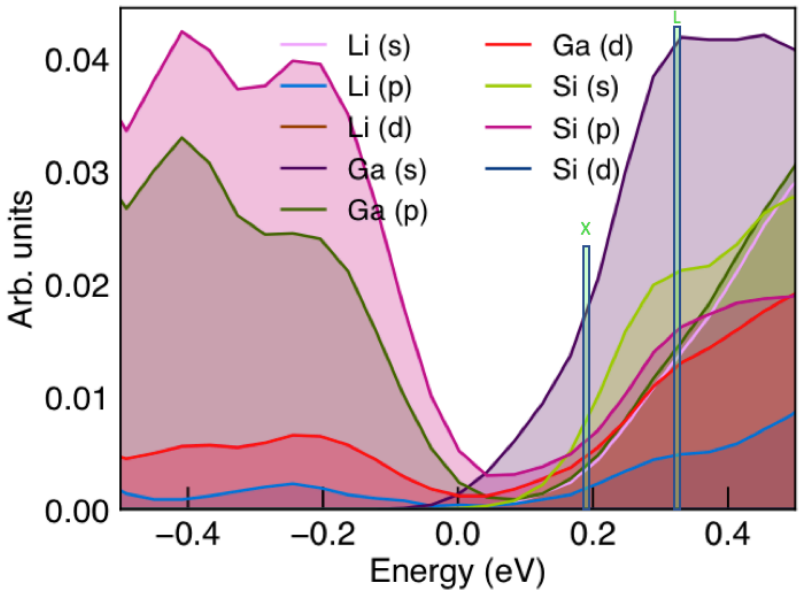


Figure 23 : Density of state of LiGaSi with detailed orbital contributions for each atom. The pocket bottom locations are shown in green. See annex D for the plotted bande-dos figures.

One can see that the Li atoms contribute the less in both X and L pockets compared to the other two elements. We thus expect the substitution of Li in this alloy to be the safest approach. In the next section, we are going to test various modification in the structure, starting by replacing some Li with Na before looking at the other 2 elements.

### 6.3.3 Substitutions

To investigate a small proportion of change in LiGaSi, it is more convenient to work within a supercell. The primitive cell of LiGaSi only contains 4 atoms of each species ($Li_4Ga_4Si_4$) which is not that suitable if we want to try some slight substitutions. In this system, the replacement of only 1 atom would lead to a substitution percentage of 25%. By increasing the system to a 2x2x2 supercell, the system becomes quite larger ($Li_{32}Ga_{32}Si_{32}$) but gives us the opportunity to work with 3% increments instead. The only drawback with this approach is the increasing of computational time for the calculations.

To increase the volume of LiGaSi, three substitutions are proposed. In each case, we replace one atom by its closer heavier neighbor in the same family. It is indeed crucial to conserve the chemistry of the material. This leaves us with three different possibilities: Li->Na, Ga->In and Si->Ge.

*1) Li->Na*

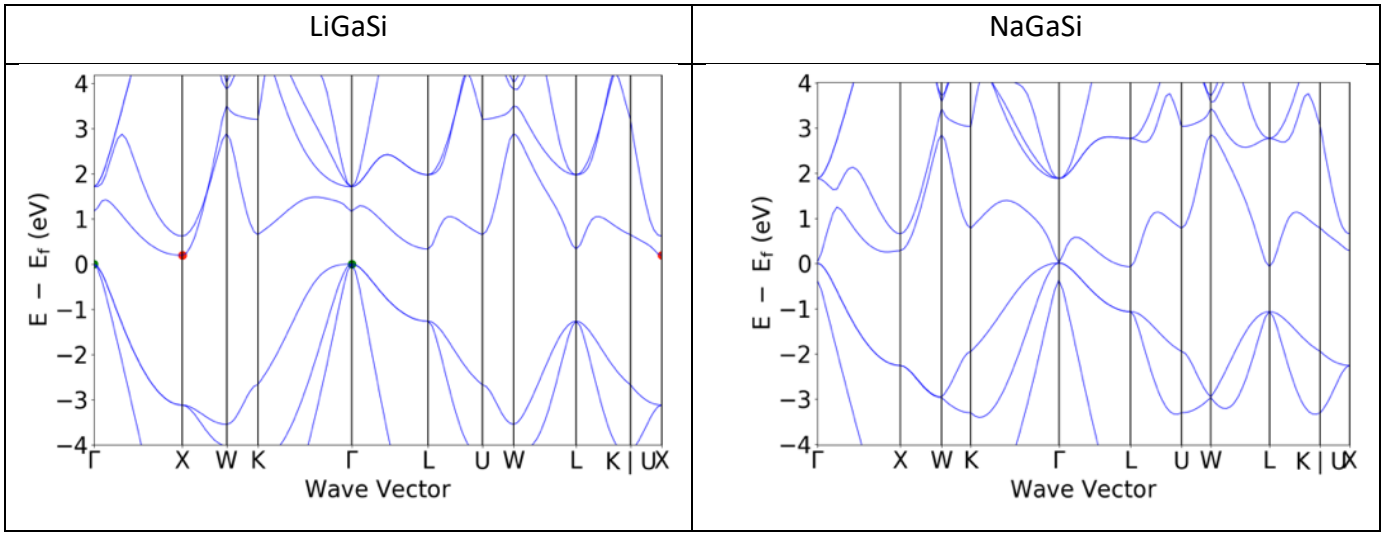


Figure 24 : Bandstructure of the alloy before and after the complete substitution Li->Na.

We can notice from Fig. 24 that the two bandstructures exhibits a nearly equivalent profile with a significant modification at the $\Gamma$ point and slight around the pockets. When Na is added to the structure, the L pocket is shifted downward while the one in X goes slightly upward. Despite the fact that NaGaSi is no longer a semiconductor, due to the disappearance of the band-gap, the mixed compounds (Li/Na)GeSi appear to conserve a band-gap (see annex H).

As it seems that we are in the right track, our next concern is to determine the optimal ratio of substitution. Previously, we stated that the $V_{opt}$ should be around 2% to 5% superior to $V_0$. If this assumption is correct in pure LiGaSi, it may not be as accurate for the mixt alloys (Li/Na)GaSi. Hence, we decided to compute the PF at several key ratios (0-25-50-100%) of substitution. The results lie in the figure bellow.

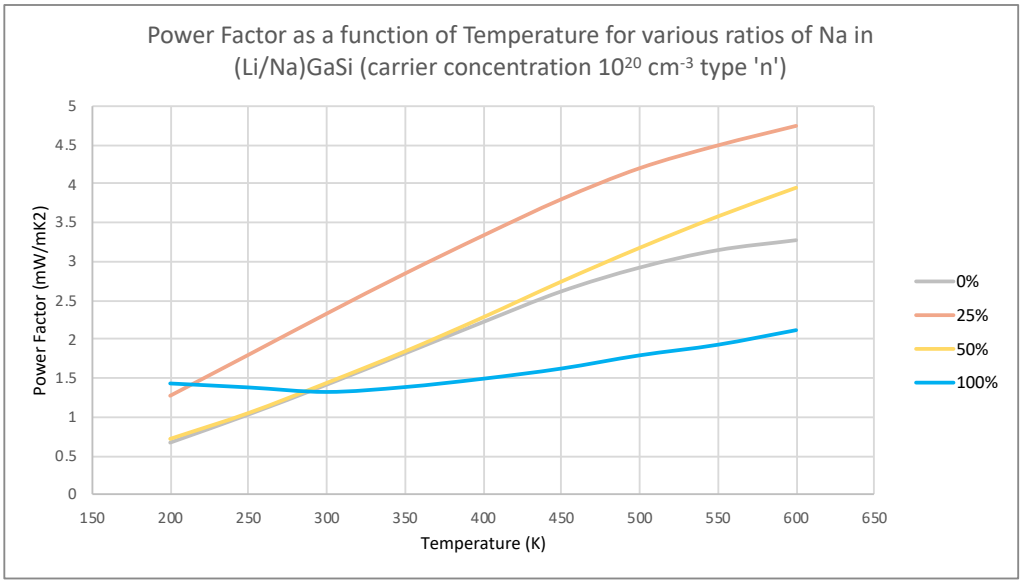


Figure 25 : First look at the PF for various substitution Li -> Na in LiGaSi.

From this graphic, we can notice a clear improvement of PF (1,4 -> 2,3 at 300K) when Na is added to the structure.

The PF first increases at 25% of Na before plummeting under its original value when higher ratios are used. Next, we conducted more analysis with a finer grid of volume on the section between 0% and 25% to get a better idea on how the PF enhancement actually works. The results are shown in Fig. 26.

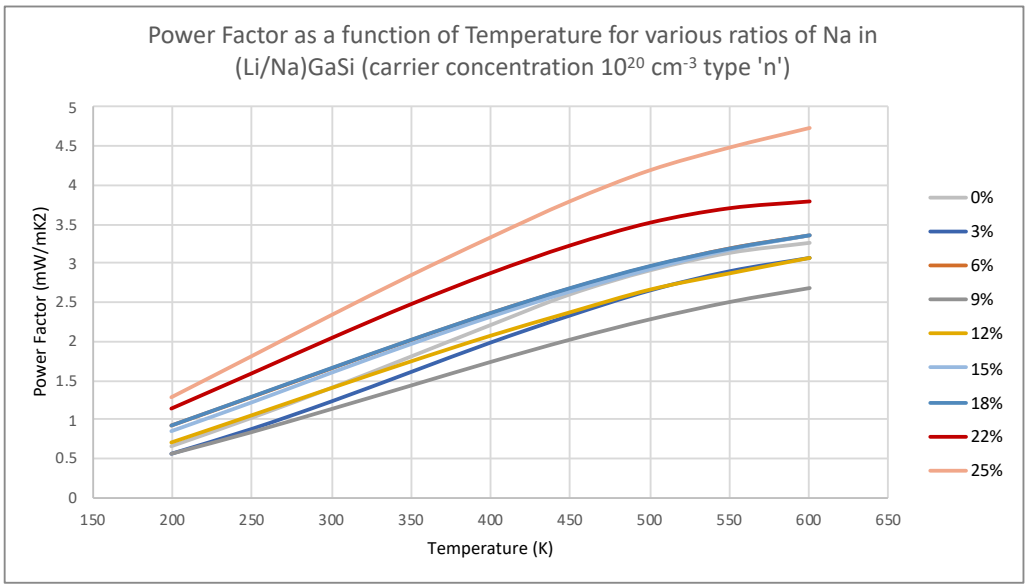


Figure 26 : PF for various percentage of Na added to the structure by replacing Li. The maximum value is set around 25%

We can notice that the PF decreases between 0% -> 9% before rising up. The substitution is efficient above 15% since the PF of the mixt alloy becomes better than the one calculated for pure LiGaSi.

At the end of the day, we still manage to get a net improvement of PF in LiGaSi with the Li/Na substitution. The results obtained with 25% of Na (band-gap: 0,2 eV) are similar to those observed for a volume increase of 2%, as shown in the next table.

*Table 6 : computed Power Factors at 300K in LiGaSi alloys.*

| Material | PF ($mW/mK^2$) |
|---|---|
| LiGaSi $V_0$ | 1,4 |
| LiGaSi V+2% | 2,3 |
| $(Li_{0,75}Na_{0,25})GaSi$ | 2,3 |

The success of Li->Na replacement lies in the low contribution of Li around the band-gap, as previously mentioned in the DOS analysis (Fig. 23). This means that the substitution has little effect on the electronic structure of the material and is therefore closer to an “only-volume” change. This would certainly not be the case for Ga and Si.

### *2) Ga->In*

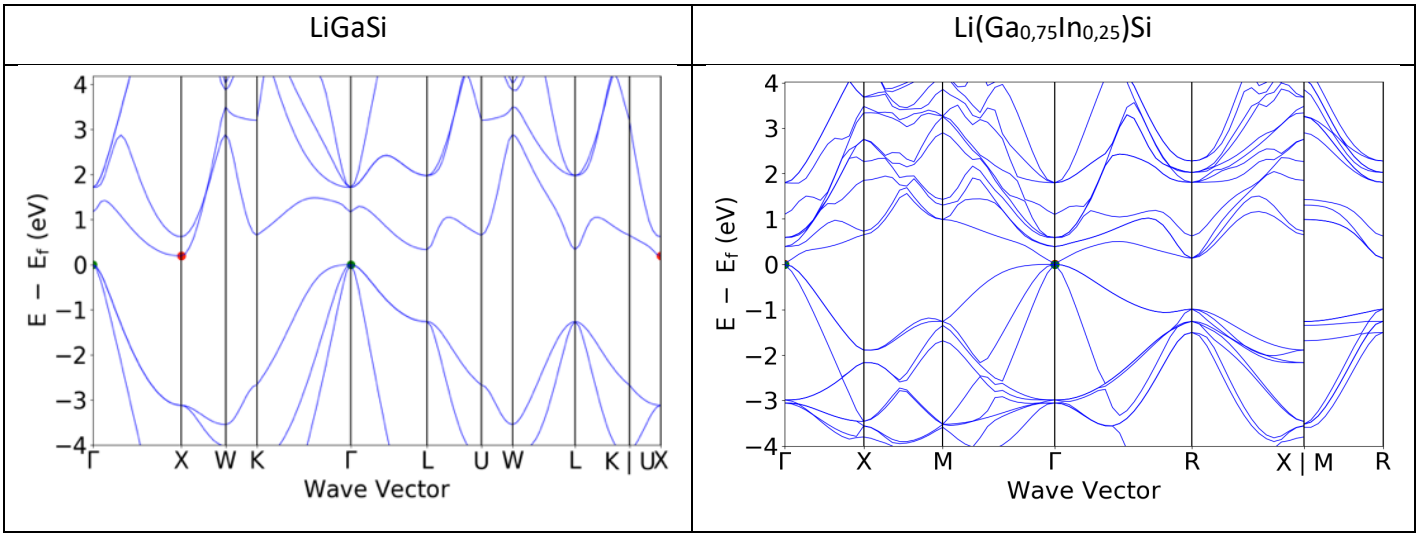


Figure 27 : Bandstructure of the alloy before and after the substitution of 25% Ga->In.

Since we had good results for a 25% of substitution in the previous section (Li -> Na), we reused the same ratio to compute the bandstructure. However, Ga->In substitution quickly encountered the same band-gap closure (see Fig. 27) as the one observed in YNiBi. This phenomenon occurred when the Γ pocket is lowered in energy.

When looking at the PF, our computations with a substitution ratio of 25% showed a net decrease of PF compared to the original structure (LiGaSi). We also investigated lower ratios at 12% ad 18% without noticing any PF improvement. The enhancement is a priori possible but would require lower ratios.

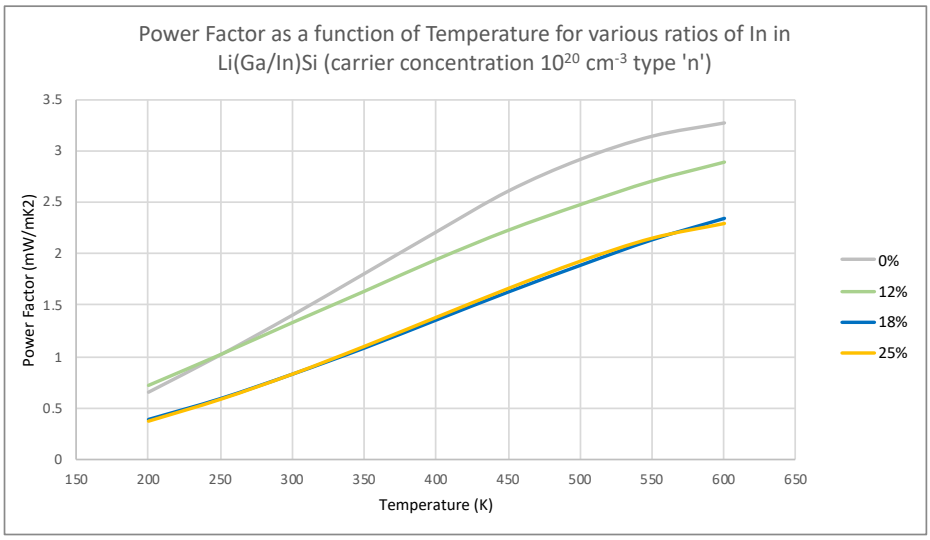


Figure 28 : PF for various percentages of In added to the structure by replacing Ga.

### *3) Si->Ge*

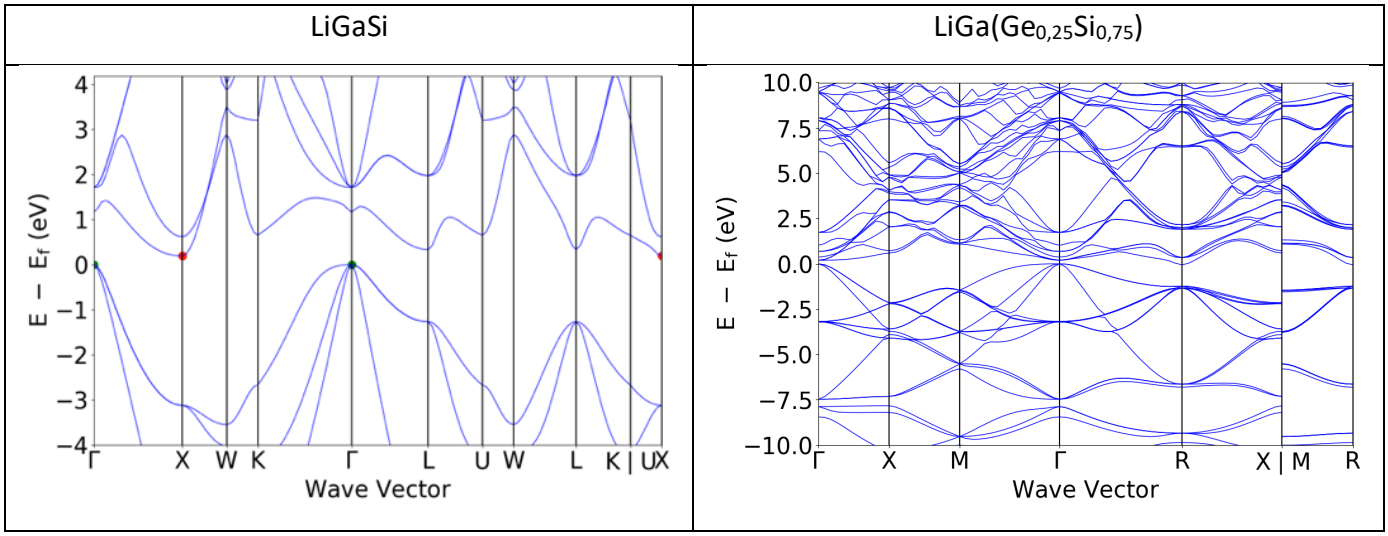


Figure 29 : Bandstructure of the alloy before and after the substitution of 25% Si->Ge.

In Si->Ge substitutions, we once again noticed the band gap closure around the Γ point (Fig. 29). The PF computations showed again inferior values compared to the original structure LiGaSi.

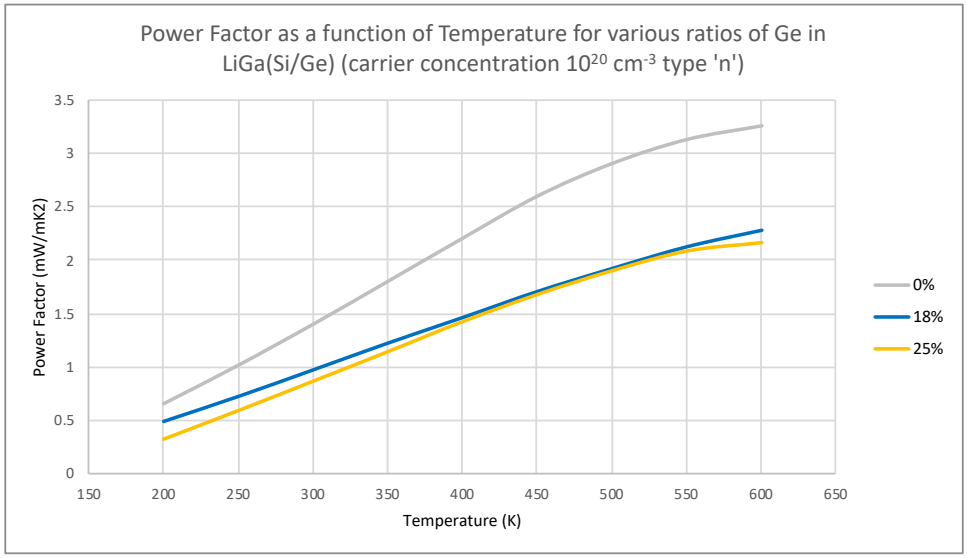


*Figure 30 : PF for various percentage of Ge added to the structure by replacing Si.*

To determine precisely which PF enhancement could be achieved for Ga->In and Si->Ge substitutions, other level of theory should be used to calculate the bandstructure. Although band-gap closures can be observed from the bands in Ga->In and Si->Ge cases, it may not be accurate given the tendency of GGA to underestimate band-gap values. Here, we are confronted to the theoretical limits of DFT calculations.

# 7. Conclusion

The energy production has proven to be an important vector of innovation and a stimulating topic for scientific research. Many approaches have tried over the years to address this fundamental challenge and the design of new thermoelectric devices are part of that process. If it was possible to efficiently recover all the wasted heat into electricity through their use, we could supply several times the world energetic demand. Although it is impossible to reach a 100% recovery ratio, due to thermodynamic limitations, a large portion of this energy is still available.

It has been almost 30 years that the computational chemistry is screening across the periodic table to find the holy grail: a cheap TE material with the highest ZT possible that would be sufficiently efficient (>10% recovery), harmless to health, and stable at the operating temperature.

Meanwhile, methods have been developed to improve the TE properties of semi-conductors. In this work, we illustrated how such enhancement could be achieved with volumetric band alignment. The VBA has this advantage to circumvent the various paradoxical effects related to the strong correlation between S, $\sigma$ and $\kappa$ occurring in TE materials. Thanks to this approach, PF improvements were performed on LiGaSi alloys without any counterpart.

For this particular case, we only explored one substitution at a time to investigate the influence of each separated modification. Further optimizations could certainly be achieved with cross-substitutions or by trying other elements for the volume distortion (Si->Sn or Li->K...).

That being said, the screening and design of TE material are integrally linked one to another. And there is no doubt that recent discovery of materials ($Fe_2V_{0,8}W_{0,2}Al$) with zT>5[43], combined to progresses made in TE enhancement will open the way to practical solutions for energy recovery.

# 8. Annexes

## Annex A : Geometrical data

| | a (Å) | b (Å) | c (Å) | α (°) | β (°) | ϒ (°) |
|---|---|---|---|---|---|---|
| $Ca_2Si$ | 7,619 | 4,818 | 9,044 | 90 | 90 | 90 |
| $Ca_2Sn$ | 7,862 | 5,108 | 9,597 | 90 | 90 | 90 |
| $Ca_2Ge$ | 7,678 | 4,855 | 9,101 | 90 | 90 | 90 |
| $Ca_8Si_3Sn$ | 7,663 | 4,883 | 9,196 | 90 | 90 | 90 |
| $Ca_8Si_3Ge$ | 7,632 | 4,836 | 9,070 | 90 | 90 | 90 |
| $Ca_8Ge_3Sn$ | 7,887 | 5,040 | 9,475 | 90 | 90 | 90 |

Table 7 : Unit cell parameters for Ca2Si and derivates.

| | a (Å) | b (Å) | c (Å) | α (°) | β (°) | ϒ (°) |
|---|---|---|---|---|---|---|
| MgTe2 | 7,109 | 7,109 | 7,109 | 90 | 90 | 90 |
| YNiBi | 4,594 | 4,594 | 4,594 | 60 | 60 | 60 |

Table 8 : Unit cell parameters for candidats selected in the Material Project database.

| | a (Å) | b (Å) | c (Å) | α (°) | β (°) | ϒ (°) |
|---|---|---|---|---|---|---|
| LiGaSi | 4,163 | 4,163 | 4,163 | 60 | 60 | 60 |
| NaGaSi | 4,441 | 4,441 | 4,441 | 60 | 60 | 60 |

Table 9 : Unit cell parameters for LiGaSi and derivates.

## Annex B : Volumetric Band Alignment in $Ca_2Si$ alloys

Table 10 : Energy variations of pockets in Ca2Si at different volumes.

| Volume (Å3) | Scaling factor | Energy at Γ (eV) | Energy at Γ-X (eV) | Energy at U (eV) | ΔEnergy Γ/Γ-X | ΔEnergy Γ/U |
|---|---|---|---|---|---|---|
| 242,08 | 0,73 | 0,0823 | 0,6412 | 0,5275 | 0,5589 | 0,4452 |
| 267,10 | 0,80 | 0,2364 | 0,6798 | 0,5825 | 0,4434 | 0,3461 |
| 298,85 | 0,90 | 0,2758 | 0,6005 | 0,523 | 0,3247 | 0,2472 |
| 315,46 | 0,95 | 0,2892 | 0,5625 | 0,4941 | 0,2733 | 0,2049 |
| 325,42 | 0,98 | 0,2947 | 0,5402 | 0,4769 | 0,2455 | 0,1822 |
| 332,05 | 1,00 | 0,2887 | 0,5185 | 0,4574 | 0,2298 | 0,1687 |
| 338,71 | 1,02 | 0,3035 | 0,5147 | 0,4583 | 0,2112 | 0,1548 |
| 348,67 | 1,05 | 0,3028 | 0,4908 | 0,439 | 0,188 | 0,1362 |
| 365,25 | 1,10 | 0,3054 | 0,458 | 0,4139 | 0,1526 | 0,1085 |
| 406,80 | 1,23 | 0,3028 | 0,383 | 0,3569 | 0,0802 | 0,0541 |
| 441,98 | 1,33 | 0,0828 | 0,3236 | 0,3093 | 0,2408 | 0,2265 |

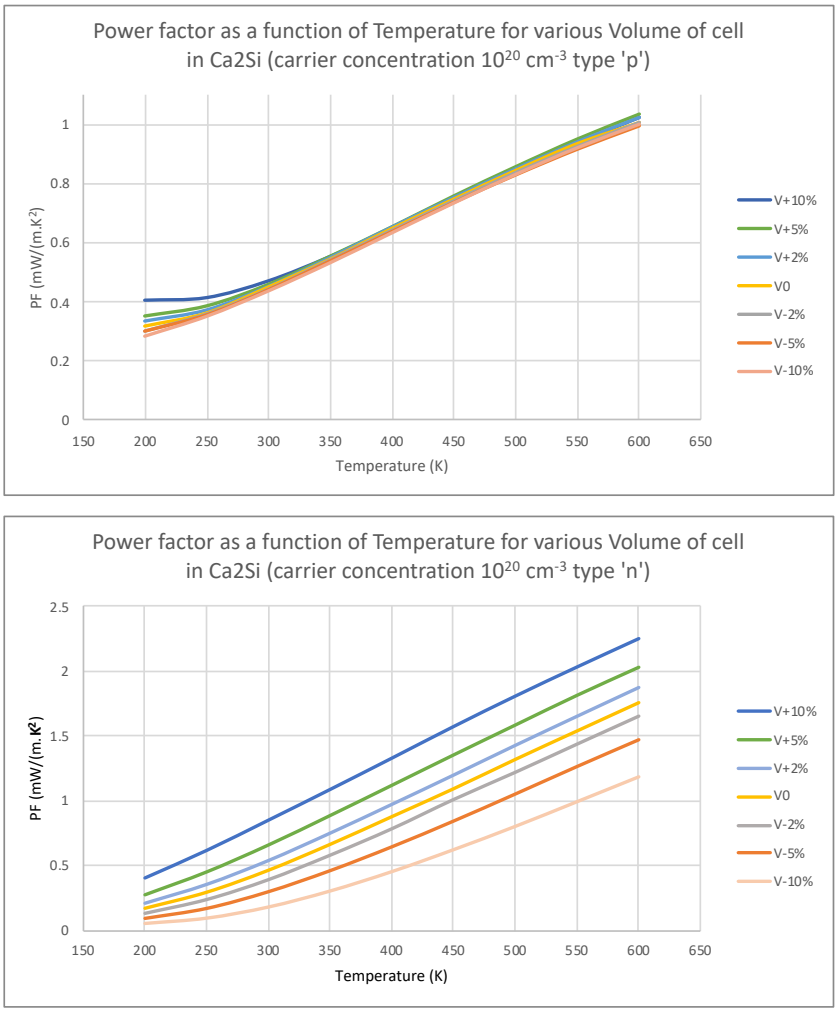


*Figure 31 : Variation of Power factor in Ca2Si at different volumes with p-doping and n-doping.*

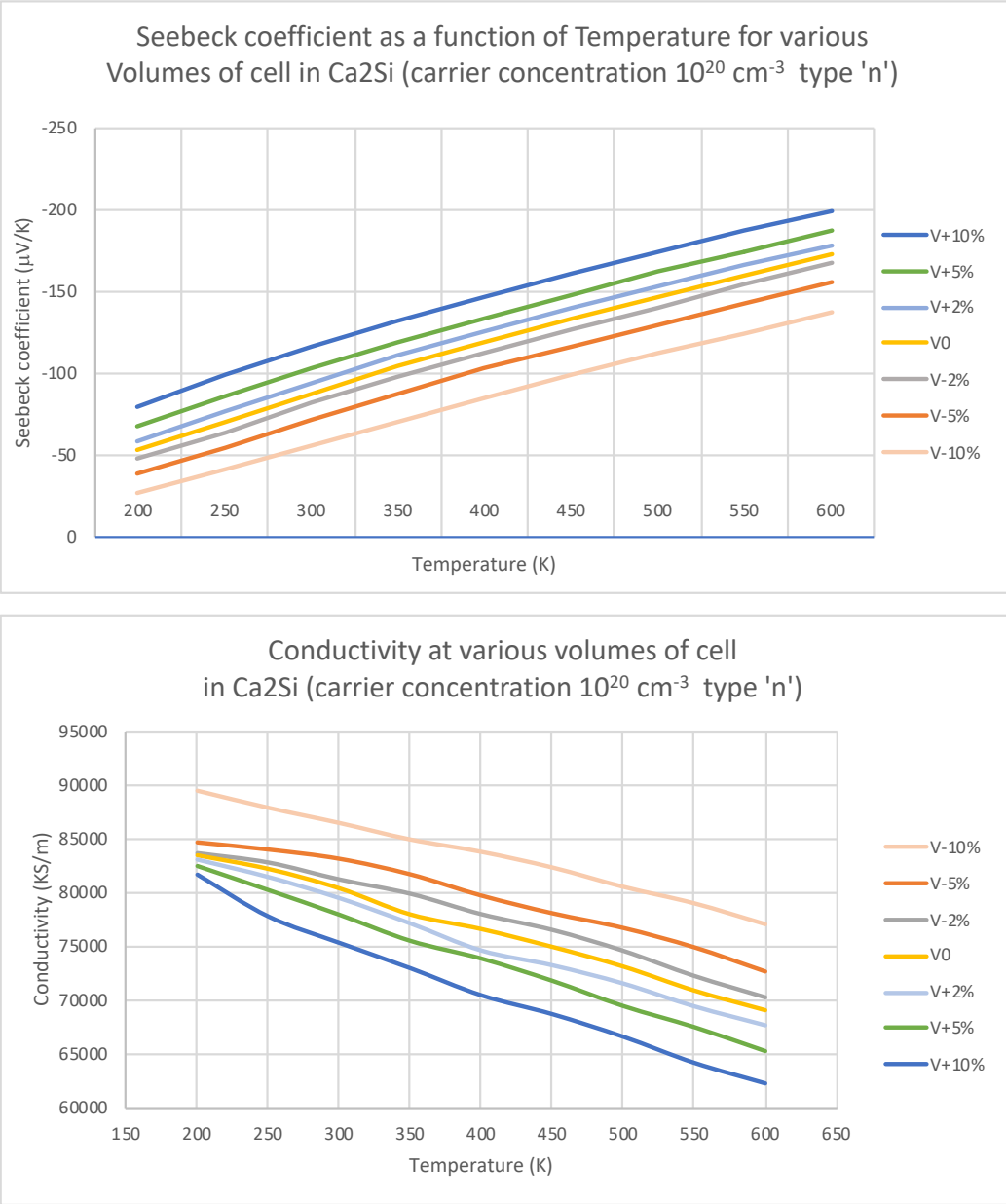


Figure 32 : Seebeck coefficient and electrical conductivity for various volumes in $Ca_2Si$.

## Annex C : Pocket alignment in LiGaSi, $MgTe_2$ and YNiBi

Table 11 : Compilation of pockets energy level under a volumetric change in LiGaSi, $MgTe_2$ and YNiBi.

| LiGaSi | Volume ($Å^3$) | Pocket X | Pocket L | ΔE (p1-p2) (ev) |
|---|---|---|---|---|
| V-5% | 193,79 | 0,1209 | 0,4927 | 0,3718 |
| V-2% | 199,91 | 0,1648 | 0,394 | 0,2292 |
| V0 | 203,99 | 0,1912 | 0,3311 | 0,1398 |
| V+2% | 208,06 | 0,2151 | 0,27 | 0,0549 |
| V+5% | 218,47 | 0,2691 | 0,1239 | -0,1452 |

| MgTe2 | Volume ($Å^3$) | Pocket Γ | Pocket Γ-R | ΔE (p1-p2) (ev) |
|---|---|---|---|---|
| V-5% | 341,29 | 1,0039 | 1,1848 | 0,1809 |
| V-2% | 352,07 | 1,0758 | 1,1926 | 0,1168 |
| V0 | 359,26 | 1,1160 | 1,1931 | 0,0771 |
| V+2% | 366,44 | 1,1552 | 1,1927 | 0,0375 |
| V+5% | 377,22 | 1,2178 | 1,1940 | -0,0238 |

| YNiBi | Volume ($Å^3$) | Pocket X | Pocket Γ | ΔE (p1-p2) (ev) |
|---|---|---|---|---|
| V-5% | 259,54 | 0,2191 | 0,8868 | 0,6677 |
| V-2% | 267,74 | 0,2097 | 0,6289 | 0,4192 |
| V0 | 273,21 | 0,2005 | 0,4688 | 0,2683 |
| V+2% | 278,67 | 0,1962 | 0,3190 | 0,1228 |
| V+5% | 286,87 | 0,1823 | 0,1073 | -0,075 |

## Annex D : Bandstructure and associated DOS for LiGaSi, $MgTe_2$ and YNiBi

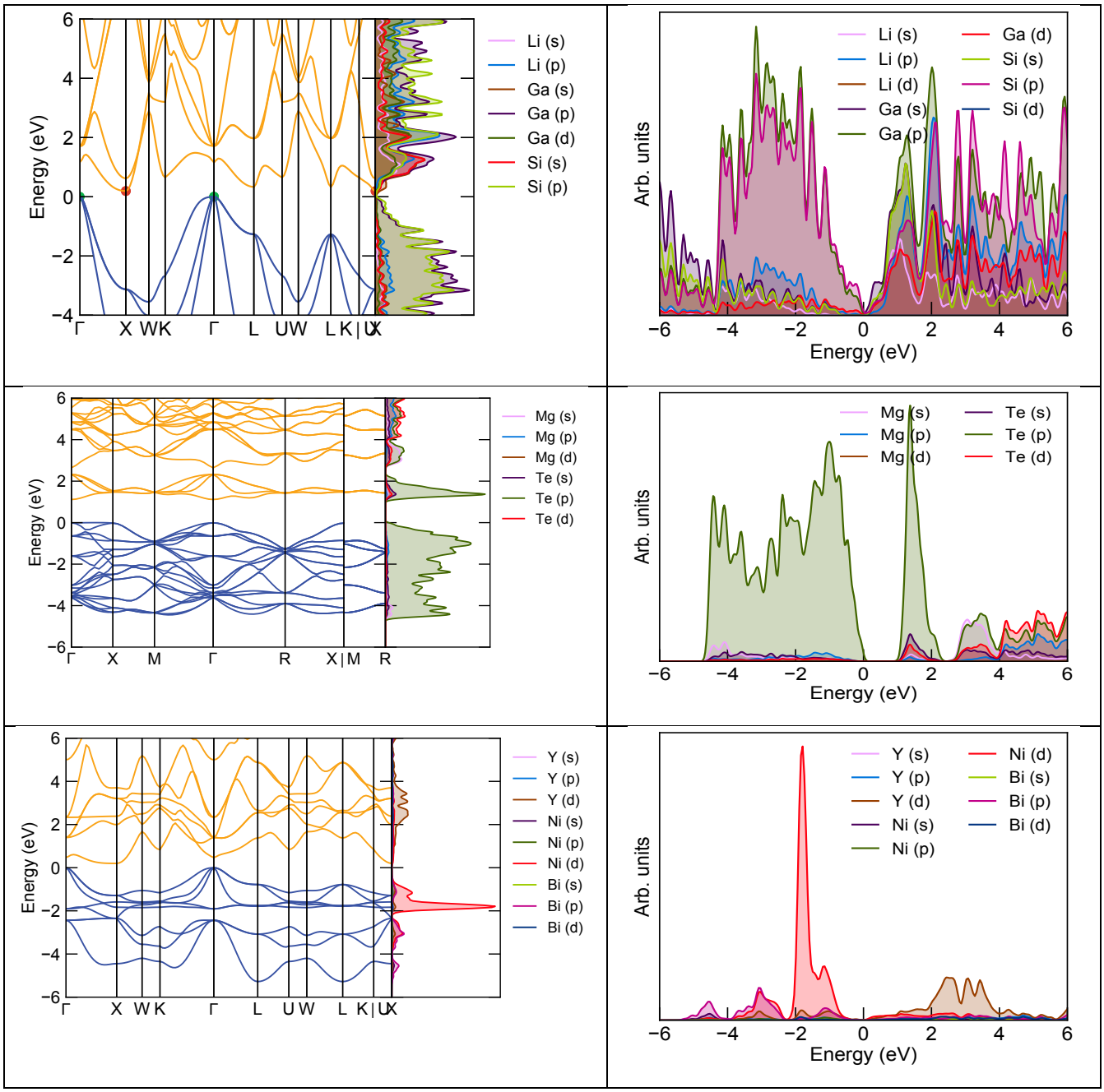


*Figure 33: From top to bottom: Bandstructure and DOS of LiGaSi, $MgTe_2$ and YNiBi.*

## Annex E : Seebeck coefficient and conductivity for LiGaSi, $MgTe_2$ and YNiBi

Table 12 : Evolution of Seebeck coefficient and electrical conductivity under a volumetric change in LiGaSi, MgTe2 and YNiBi.

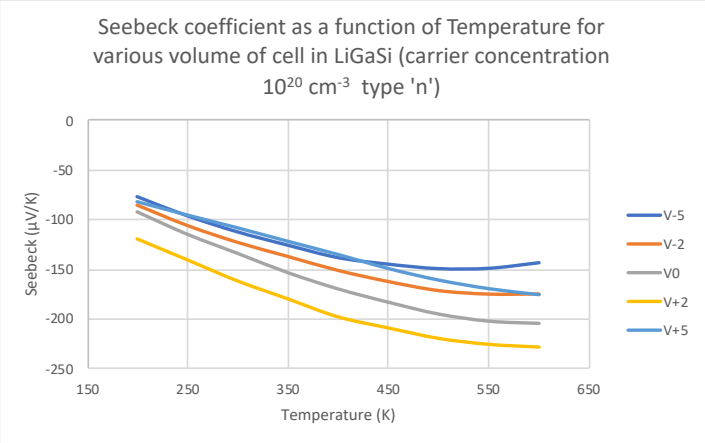


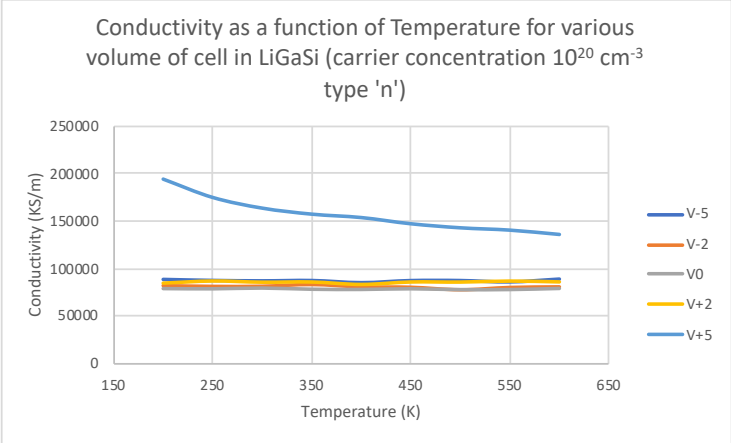


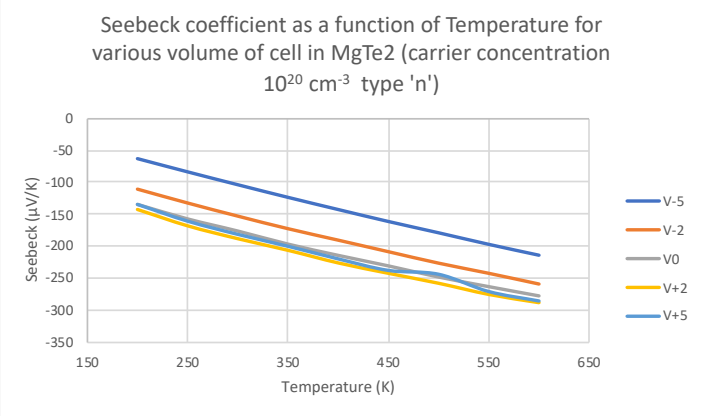


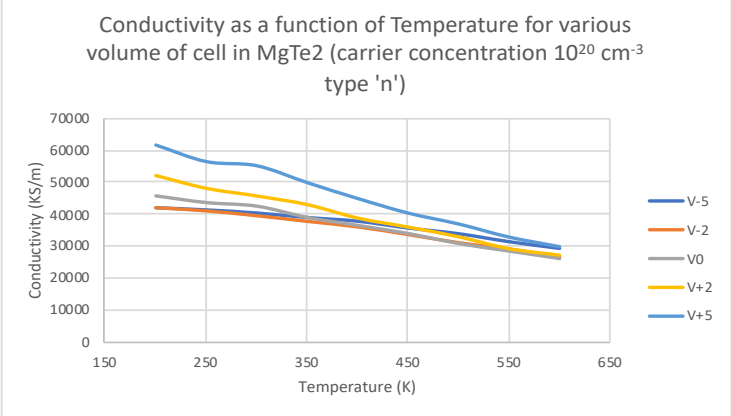


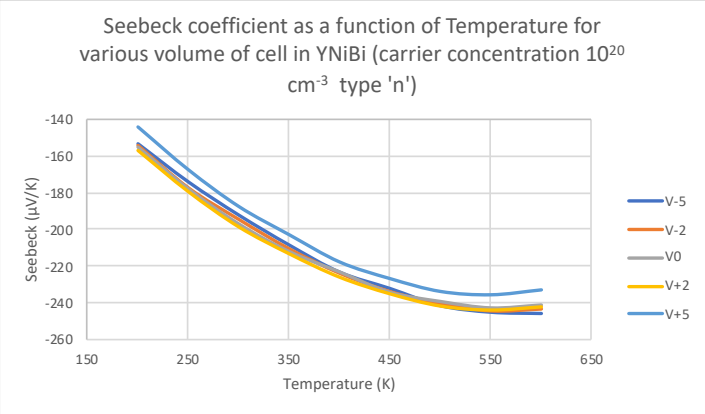


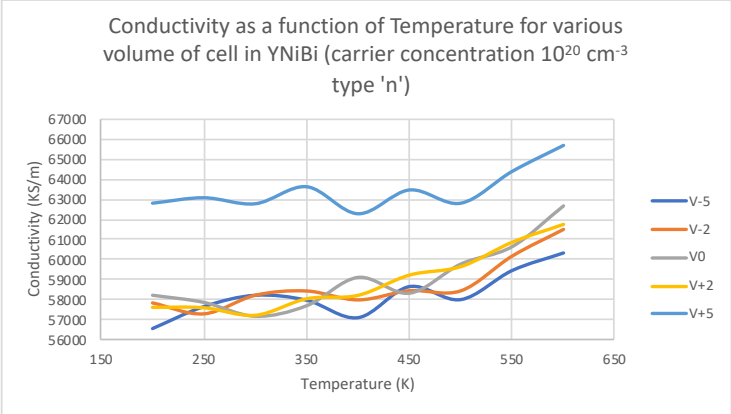

## Annex F : Power Factor of LiGaSi and $MgTe_2$ at other carrier concentrations

Table 13 : Power factor for LiGaSi and $MgTe_2$ with carrier concentration of $10^{19}$ and $10^{20}$ carrier/$cm^3$.

**Power Factor for LiGaSi**

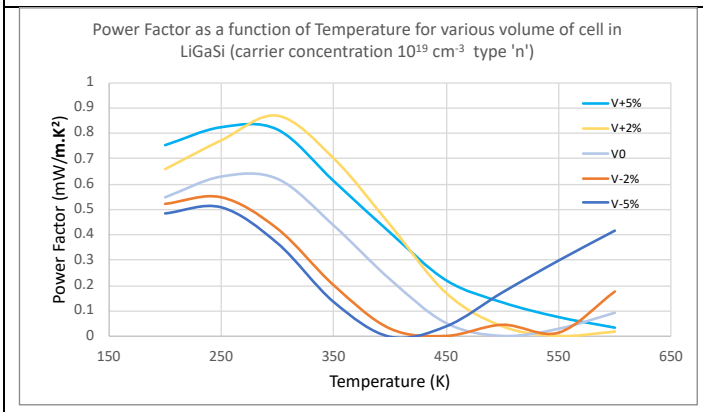


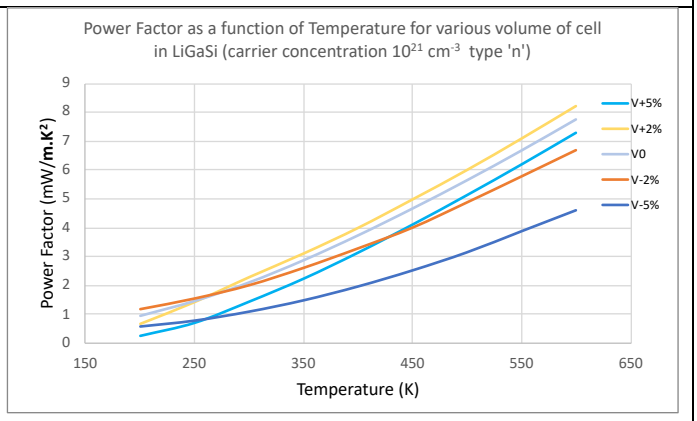


**Power Factor for $MgTe_2$**

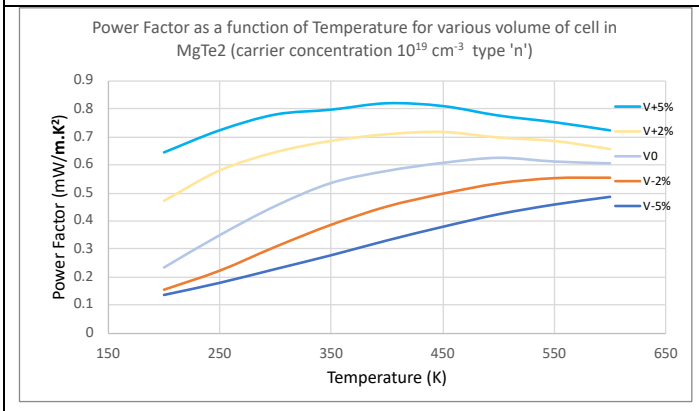


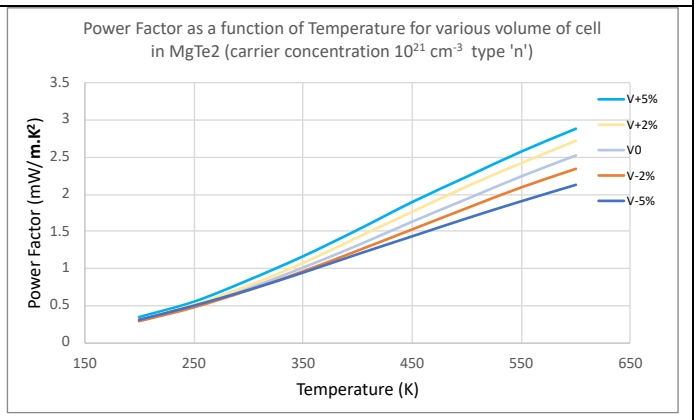

## Annex G : Volume and substitution ratio used for LiGaSi

Table 14 : Atomic composition of 2x2x2 supercells and volume for the primitive cells during the substitutions in LiGaSi.

| Ratio Na/Li | % of Na | Volume (Å$^3$) |
|---|---|---|
| 0 32 | 0% | 203,99 |
| 1 31 | 3% | 204,04 |
| 2 30 | 6% | 205,43 |
| 3 29 | 9% | 206,83 |
| 4 28 | 12% | 208,95 |
| 5 27 | 15% | 210,86 |
| 6 26 | 18% | 211,12 |
| 7 25 | 22% | 213,29 |
| 8 24 | 25% | 214,19 |
| 16 16 | 50% | 223,98 |
| 32 0 | 100% | 247,80 |

| Ratio In/Ga | % of In | Volume (Å$^3$) |
|---|---|---|
| 4 28 | 12% | 208,99 |
| 6 26 | 18% | 212,41 |
| 8 24 | 25% | 215,22 |

| Ratio Ge/Si | % of Ge | Volume (Å$^3$) |
|---|---|---|
| 6 26 | 18% | 203,09 |
| 8 24 | 25% | 208,34 |

## Annex H : Bandstructures for (Li/Na)GaSi substitutions

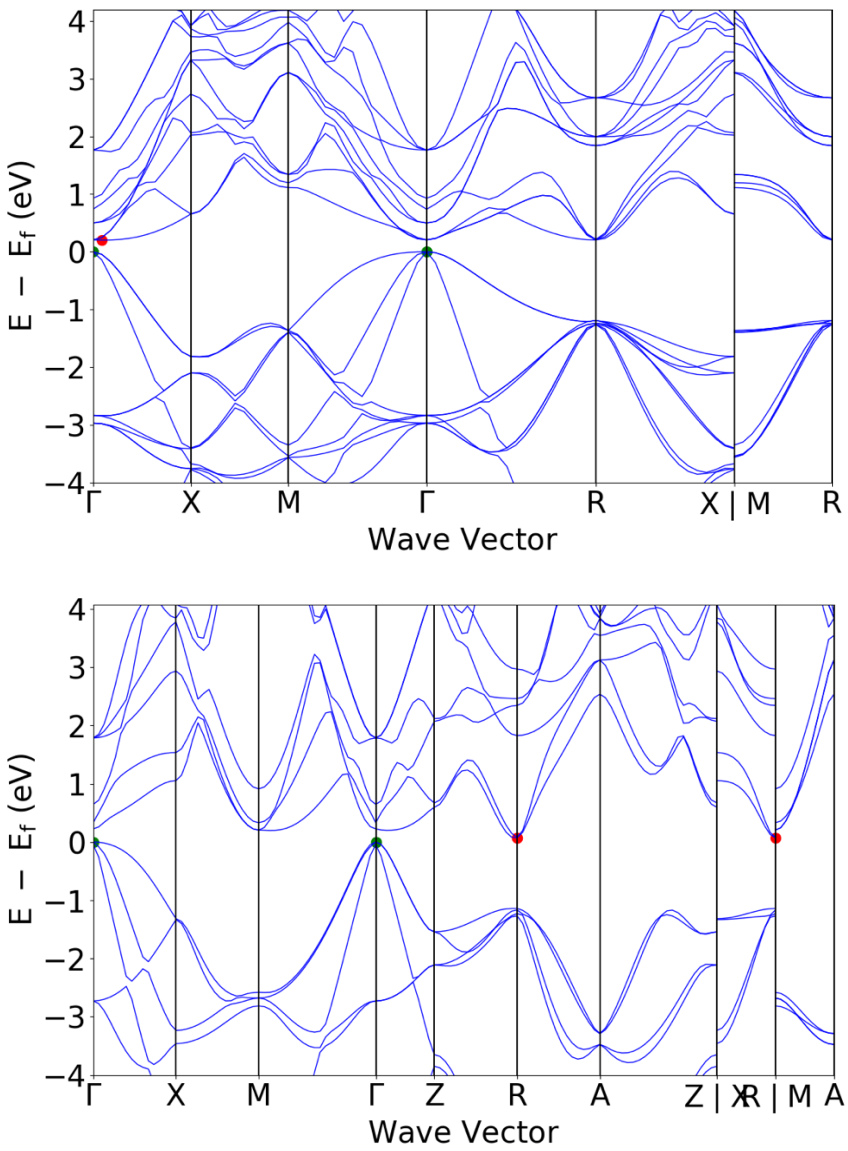


Figure 34 : Bandstructure of (Li/Na)GaSi for 25% (upside) and 50% (bellow) of Na.

# 9. Bibliography


[1] A. Jain, G. Hautier, C. J. Moore, S. P. Ong, C. C. Fischer, T. Mueller, K. A. Persson, and G. Ceder, A high-throughput infrastructure for density functional theory calculations, Computational Materials Science, Vol. 50, **2011**, p. 2295-2310.

[2] U. Bossel, Well-to-wheel studies, heating values and the energy conservation principle, Euripean Fuel Cell Forum, **2003**

[3] E. Gottzein, K-H. Brock, E. Schneider, J. Pfefferl, Control aspects of a tracked magnetic levitation high speed test vehicle, Automatica, Vol.13, May **1977**, p. 205-223

[4] D. D. Allred, Short course on thermoelectrics : An overview of thermoelectrics, International Thermoelectric Society, **1993**

[5] T.J.Seebeck, Abh. K. Akad. Wiss., Berlin, **1823**, p. 265

[6] T.M.Tritt, M.A. Subramanian, Thermoelectric materials, phenomena, and applications : A bird's eye view, MRS bulletin, Vol.31, March **2006**

[7] M. V. Vedernikov et E.K. Iordanishvili, A.F. Ioffe and origin of modern semiconductor thermoelectric energy conversion, Proceedings ICT 98, XVII International Conference on Thermoelectrics, **1998**

[8] G.J. Snyder, E.S Toberer, Complex thermoelectric materials, Nature materials, Vol.7, February **2008**

[9] A.F. May, G.J Snyder, Introduction to Modeling Thermoelectric Transport at High Temperatures, March **2016**, p. 1-16

[10] H. Hiramatsu; K.Ueda; H. Ohta; M. Hirano; T. Kamiya; H. Hosono, Wide gap p-type degenerate semiconductor: Mg-doped LaCuOSe, Proceedings of the 3rd International Symposium on Transparent Oxide Thin films for Electronics and Optics, Decembre **2003**, p. 304–308.

[11] C.J.M. Lasance, Tables of Seebeck coefficient, November **2006**, via www.electronics-cooling.com

[12] D.I. Bile, G. Hautier, D. Waroquiers, G-M. Rignanese, P. Ghosez, Low-Dimensional Transport and Large Thermoelectric Power Factors in Bulk Semiconductors by Band Engineering of Highly Directional Electronic States, Physical Review Letters, April **2015**

[13] G.K.H. Madsen, Automated Search for new thermoelectric materials : the case of LiZnSb, JACS articles, **2006**

[14] Ismail, B. I.; Ahmed, W. H., Recent Patents on Electrical & Electronic Engineering (Formerly Recent Patents on Electrical Engineering) **2009**, 2, p.27–39.

[15] A.M. Dehkordi, M.Zebarjadi, J.He, T.M.Tritt, Termoelectric power factor: Enhancement mechanisms and strategies for higher performance thermoelectric materials, Material Science and Engineering, November **2015**, p. 1-22

[16] Y.Pei, H.Wang, G.J. Snyder, Band engineering of thermoelectric materials, *Advanced materials*, Vol. 24, **2012**, p. 6125-6135

[17] M.Faizan*, H. Ullah, S.H. Khan, S.M. Ramay, S.A.S Qaid, A. Mahmood, M. Ali, Carrier effective masses and thermoelectric properties of novel $Ag_3AuSe_2$ and $Ag_3AuTe_2$ compounds, International Journal of Modern Physics, Vol. 31, **2017**

[18] H.Wang, Y. Pei, A.D.Lalonde, G.J. Snyder, Weak electron-phono coupling contributing to high thermoelectric performance in n-type PbSe, PNAS, Vol.109, June **2012**, p.9705-9709

[19] H.Wang, Y.Pei, A.D.LaLonde, G.J.Snyder, Material design considerations based on thermoelectric quality factor, Material Science, Vol.182, **2013**, Chap 1, p.17-22

[20] T.Pei, X.Shi, A. LaLonde, H. Wang, L. Chen, G.J. Snyder, Convergence of electronic bands for high performance bulk thermoelectrics, Nature, Vol. 473, **2011**, p. 66-69

[21] Y. Pei, A.D. Lalonde, H. Wang, G.J. Snyder, Low effective mass leading to high thermoelectric performance, Energy Environnement Science, **2012**, p. 7963-7969

[22] K.H. Lee, S.W. Kim, Design and preparation of High-performance nulk thermoelectric materials with defect structures, Journal of the Korean Ceramic Society, Vol 54, **2017**, p. 75-85

[23] G.Tan, Li-Dong Zhao, M.G. Kanatzidis, Rationally designing High-performance Bulk thermoelectric materials, Chemical reviews, **2016**, 116, p. 12123–12149.

[24] Z. Jinze, W. Teng, W. Hongchao, S. Wenbin, W. Xue, C. Tingting, W. Chunlei, Strategies for optimizing the thermoelectricity of PbTe alloys, Chinese Physics B, **2018**

[25] B.v.Zeghbroeck, Principles of semiconductor devices, chap. 2, **2011**

[26] P.Yu, M.Cardona, Fundamentals of Semiconductors : Physic and material properties, Springer, 4th edition, **2010**, p. 220-224.

[27] G.K.H. Madsen and S. Bhattacharya, High-throughput exploration of alloying as design strategy for thermoelectrics, Physical Review, B 92, **2015**

[28] G.K. Madsen, J. Carrete, M.J. Verstraete, BoltzTrap2, a program for interpolating band structures and calculating semi-classical transport coefficients, Computer Physics Communications, Decembre 2017

[29] A.v.Lilienfeld, lecture on quantum chemistry, **2018**

[30] Hohenberg, P.; Kohn, W. Physical review, **1964**, 136, B864.

[31] G. Hautier, LCHM1353, cursus of quantum chemistry, **2017**

[32] J.P. Perdew, Density functional theory and the band gap problem, International journal of Quantum Chemistry, Vol. 28, **1985**, p. 497-523

[33] G. Sun,J. Kürti, P. Rajczy, M. Kertesz, J. Hafner, G. Kresse, Performance of the Vienna ab initio simulation package (VASP) in chemical applications, Journal of Molecular Structure TEOCHEM, Vol. 624, **2003**, p. 37-45

[34] G.K.H. Madsen, D.J.Singh, BoltzTrap, A code for calculating band-structure dependent quantities, Elsevier Science, **2008**

[35] N.W. Ashcroft, N.D. Mermin, Solid State Physics, **1976**, chap. 13

[36] G.K.H. Madsen, J. Carrete, M.J. Verstraete, BoltzTraP2, a program for interpolating band structures and calculating semi-classical transport coefficients, Computer Physics Communications, **2018**.

[37] P.E. Blöchl, Physical Review B 50, **1994**, p. 17953-17979

[38] Computational resources have been provided by the Consortium des Équipements de Calcul Intensif (CÉCI), funded by the Fonds de la Recherche Scientifique de Belgique (F.R.S.-FNRS) under Grant No. 2.5020.11 and by the Walloon Region.

[39] Shyue Ping Ong, William Davidson Richards, Anubhav Jain, Geoffroy Hautier, Michael Kocher, Shreyas Cholia, Dan Gunter, Vincent Chevrier, Kristin A. Persson, Gerbrand Ceder. Python Materials Genomics (pymatgen): A Robust, Open-Source Python Library for Materials Analysis. Computational Materials Science, **2013**, Vol. 68, p. 314–319.

[40] Most of the bandstructures in this thesis were plotted with the sumo program: Alex M. Ganose, Adam J. Jackson, David O. Scanlon. sumo: Command-line tools for plotting and analysis of periodic ab initio calculations. Journal of Open Source Software, **2018**

[41] D. Parker and D. J. Singh, Sci. Tech. Adv. Mater., vol.14, **2013**

[42] A. Jain, S.P. Ong, G. Hautier, W. Chen, W.D. Richards, S. Dacek, S. Cholia, D. Gunter, D. Skinner, G. Ceder, K.A. Persson, The Materials Project: A materials genome approach to accelerating materials innovation, Applied Materials, **2013**

[43] B. Hinterleitner, I. Knapp, M. Poneder, Y. Shi, H. Müller, G. Eguchi, C. Eisenmenger-Sittner, M. Stöger-Pollach, Y. Kakefuda, N. Kawamoto, Q. Guo, B. Tetsuya, M. Takao, S. Ullah, X. Chen, E. Bauer, Thermoelectric performance of a metastable thin-film Heusler alloy, Nature, Vol. 576, **2019**

UNIVERSITÉ CATHOLIQUE DE LOUVAIN
**Faculté des sciences**
Place des sciences, 2 bte L6.06.01, 1348 Louvain-la-Neuve, Belgique | **www.uclouvain.be/sc**